Scientific Reports

https://doi.org/10.1038/s41598-026-50077-1

Article in Press

Regional drought forecasting in data-scarce regions through a novel cluster-based liquid neural network

Received: 29 September 2025

Accepted: 20 April 2026

Published online: 26 April 2026

Cite this article as: Danandeh Mehr A., Ghavifekr A.A. & Tur R. Regional drought forecasting in data-scarce regions through a novel cluster-based liquid neural network. *Sci Rep* (2026). https://doi.org/10.1038/s41598-026-50077-1

Ali Danandeh Mehr, Amir A. Ghavifekr & Rifat Tur

We are providing an unedited version of this manuscript to give early access to its findings. Before final publication, the manuscript will undergo further editing. Please note there may be errors present which affect the content, and all legal disclaimers apply.

If this paper is publishing under a Transparent Peer Review model then Peer Review reports will publish with the final article.

ARTICLE IN PRESS

© The Author(s) 2026. **Open Access** This article is licensed under a Creative Commons Attribution-NonCommercial-NoDerivatives 4.0 International License, which permits any non-commercial use, sharing, distribution and reproduction in any medium or format, as long as you give appropriate credit to the original author(s) and the source, provide a link to the Creative Commons licence, and indicate if you modified the licensed material. You do not have permission under this licence to share adapted material derived from this article or parts of it. The images or other third party material in this article are included in the article's Creative Commons licence, unless indicated otherwise in a credit line to the material. If material is not included in the article's Creative Commons licence and your intended use is not permitted by statutory regulation or exceeds the permitted use, you will need to obtain permission directly from the copyright holder. To view a copy of this licence, visit http://creativecommons.org/licenses/by-nc-nd/4.0/.

ARTICLE IN PRESS

Regional drought forecasting in data-scarce regions through a novel cluster-based liquid neural network

Ali Danandeh Mehr[1], Amir A. Ghavifekr [2], Rifat Tur[3]

[1]Department of Civil Engineering, Antalya Bilim University, Antalya, Türkiye.

[2]Faculty of Electrical and Computer Engineering, University of Tabriz, Tabriz, Iran.

[3]Department of Civil Engineering, Faculty of Engineering, Akdeniz University, Antalya, Türkiye

Corresponding author: aa.ghavifekr@tabrizu.ac.ir

ARTICLE IN PRESS

Abstract: The Global Drought Monitor (GDM) provides real-time information about drought to enhance drought forecasting; however, applying complex machine learning algorithms across large spatial domains is computationally challenging. This study presents a novel approach for one-month-ahead regional drought forecasting using GDM data. The new approach first uses k-means to cluster GDM grid points into homogeneous regions based on their geographic coordinates (latitude, longitude, and elevation) and temporal variation of the Standardized Precipitation-Evapotranspiration Index (SPEI) series. Then, a cluster representative SPEI series ($SPEI_{cr}$) is generated for each cluster, and is targeted for modeling and forecasting using the state-of-the-art liquid neural network (LNN) technique.

ARTICLE IN PRESS

To achieve the best forecasting accuracy, the univariate and multivariate LNN models are configured by the most effective lags of $SPEI_{cr}$ and exogenous inputs chosen among the GDM-SPEI series that show the minimum Euclidean distance to each cluster centroid in both the geographic and feature spaces. Based on the superior performance of the multivariate LNN, the $SPEI_{cr}$ forecasts are ultimately extended across all GDM points in the corresponding homogenous region to map future regional drought patterns. The new approach was demonstrated through a case study conducted for the Lake Urmia Basin (LUB), which suffers from both frequent prolonged meteorological droughts and scarce long-term ground truth data. The results showed that a rigorous spatially adaptive drought forecasting map can be delineated across LUB via the proposed model. Notably, the LUB was clustered into five drought-homogenic clusters where multivariate LNN models showed, on average, more than 100% and 40% performance improvement in terms of Nash-Sutcliffe efficiency over the univariate LNN and Seasonal Auto Regressive Integrated Moving Average benchmarks, respectively. This corresponded to an average root mean squared error of 0.25 for the multivariate models, whereas the benchmark errors remained higher, at approximately 0.54 and 0.72, respectively.

Keyword: regional drought, mapping, forecasting, liquid neural network, k-means, SPEI, Lake Urmia

ARTICLE IN PRESS

ARTICLE IN PRESS

1. Introduction

Drought is one of the most critical global environmental challenges, exerting severe socio-economic and ecological impacts, particularly across the Middle East [1-3]. Effective drought monitoring and forecasting are essential for sustainable water resources management, supporting the development of drought vulnerability maps and operational early warning systems [4-6]. However, conventional statistical forecasting methods often struggle to adequately represent short-term drought variability, mainly due to the stochastic, nonlinear, and non-stationary nature of hydro-climatic processes under changing climate conditions [7-9]. To overcome these limitations, advanced machine learning (ML) and deep learning (DL) techniques have emerged as powerful alternatives for drought modeling and forecasting [10-16]. For instance, Mokhtar et al. [13] developed four ML and DL models, including convolutional neural networks (CNN), extreme gradient boosting (XGB), random forest (RF), and long short-term memory (LSTM), to estimate Standardized Precipitation Evapotranspiration Index (SPEI) at 3- and 6-month aggregation across Qinghai–Tibet Plateau, China. The models showed varying performance in different scenarios with less accuracy for SPEI-3 forecasts. In another study, Adikari et al. [17] compared performances of three ML models, namely CNN, LSTM, and wavelet-based Adaptive Neuro-Fuzzy Inference System (WANFIS), for unit-times ahead drought forecasting using Standardized Precipitation Index (SPI) at eight meteorology stations in Australia. The authors demonstrated that WANFIS performed better than its

ARTICLE IN PRESS

counterparts. In a similar study, Altunkaynak and Çelik [18] suggested a hybrid additive season algorithm-Fuzzy Inference System model for drought forecasting in Van, Ankara, and Istanbul meteorology stations. The authors showed that the new hybrid algorithm outperforms WANFIS for longer forecasting time horizons. More recently, Danandeh Mehr et al. (2025) [19] compared the prediction accuracy of three ML models, namely, Multilayer Perceptron, LSTM, and Transformer Encoders (TE), for SPI prediction at two meteorology stations in Turkey. The authors demonstrated that a sequential-based TE can achieve the highest prediction accuracy.

A major challenge in the aforementioned studies is their reliance on station data, which leads to station-based models with accuracy that varies across a hydrologic basin. Consequently, generating a basin-scale drought vulnerability map requires developing separate ML or DL models for each station. This approach is impractical in regions with sparse measurement networks. Furthermore, interpolating point forecasts across ungauged regions can introduce significant uncertainties due to complex local hydro-climatic conditions and the various triggers influencing drought indicators [20]. To address these limitations, regional drought forecasting (RDF) often employs high-resolution satellite-based or reanalysis environmental monitoring tools, such as APHRODITE, TRMM, CHIRPS, NASA GISS, and ERA5 [21-23]. The availability of such datasets has created significant opportunities for enhancing drought monitoring and forecasting in both

ARTICLE IN PRESS

temporal and spatial dimensions [24]. However, leveraging this potential with advanced ML/DL algorithms is computationally expensive when applied to each grid cell over large domains [25-26]. This expense limits the scalability and practical application of these models, particularly in resource-constrained settings. An additional challenge is that identifying the most effective predictors and optimal ML models requires extensive data processing and often necessitates intercomparisons between influencing predictors and techniques [11,27]. Therefore, balancing computational efficiency with the need to capture spatial heterogeneity remains a critical challenge in drought forecasting [28].

This paper introduces a novel DL approach designed to overcome the computational challenges of large-domain RDF, particularly in data-scarce regions. The new approach directly utilizes real-time gridded SPEI dataset from the Global Drought Monitor (GDM). It employs a k-means clustering algorithm to group similar grid cells based on geographic and temporal SPEI characteristics. By partitioning the domain into clusters, each represented by a centroid, robust multivariate Liquid Neural Network (LNN) models are trained exclusively on these representative SPEI series, substantially reducing the computational cost. Once trained, the forecasts generated for the centroids are transferred to all grid points within their respective clusters. This strategy effectively captures the spatial variability of drought

ARTICLE IN PRESS

conditions while maintaining computational efficiency, offering a scalable and practical solution for regional drought prediction.

Although a few previous studies have suggested clustering-based drought maps, they relied on a limited number of in situ stations [5,29]. To the best of our knowledge, this is the first study to introduce a cluster-based LNN framework for basin-scale drought forecasting and mapping. The proposed model was applied to generate one-month lead regional SPEI forecasts across the Lake Urmia Basin (LUB) in Iran. Given the sensitivity of ML models to input variables, both univariate LNN (hereafter ULNN) and multivariate LNN (hereafter MLNN) models were configured and compared to identify the most relevant predictors for drought forecasting within each cluster.

ARTICLE IN PRESS

2. Study area and data

2.1. Lake Urmia Basin (LUB)

The LUB located between the provinces of East Azerbaijan, West Azerbaijan, and Kurdistan in the northwest of Iran, with an area of 52×10^3 km^2 (Figure 1). The annual average precipitation and evaporation LUB are approximately 350 mm and 900-1170, respectively [30]. The average temperature is about 11.2°C, with average minimum and maximum temperatures at 2.5°C (January) and 23.9°C (July), respectively [31]. In recent decades, the drop in water level of the lake has been one of the most important environmental issues in Iran. Lake Urmia's basin is currently facing severe threats due to a

ARTICLE IN PRESS

significant decline in the lake's water level, leading to increased salinity [32]. Due to the significant decrease in the lake's level, surface area, and the surrounding groundwater level, drought monitoring and forecasting in LUB were considered as a hot topic in the regional studies. According to the authors' field survey in August 2025, the lake level has dropped by about 99% and the lake is on the brink of disappearing. Nevertheless, the public and the government's national determination to save the lake is not impressive. The most important action would be charging the lake with surface water captured from the basin. Despite numerous studies, there is still an ambiguity about the main cause of this disaster. Environmental bodies consider the dam building on upstream rivers and expansion of irrigated agricultural area as the main factors, while the water companies claim that climate change and less precipitation are the primary reasons [30,33].

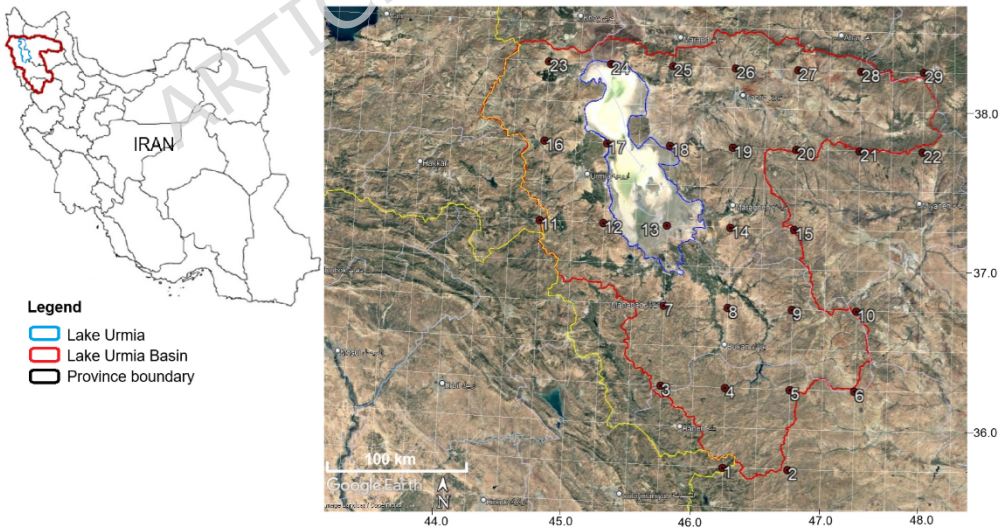


Figure 1. The Lake Urmia Basin including 29 Global Drought Monitor grid points across LUB (The map was generated using Google Earth Pro_7.3.71155).

ARTICLE IN PRESS

2.2 Dataset

We used the GDM dataset [34], which provides long-term real-time SPEI with a 0.5 degree spatial resolution and a monthly time resolution. The SPEI series with time-scales between 1 and 48 months approximately cover the globe from 1950 to the present. The SPEI is based on monthly precipitation (P) sums and mean temperature, which are obtained from the Global Precipitation Climatology Centre (GPCC) and NOAA NCEP CPC GHCN_CAMS gridded dataset, respectively [35].

In this study, 3-month SPEI time series (hereafter SPEI-3), a short-term aggregation, from 1951 (March) to 2025 (May), a total of 903 months, at 29 GDM grid points across LUB (Figure 1) were used. Table 1 summarizes the geographical locations of the implemented GDM gridpoints as well as the statistical features of the associated SPEI-3 series.

ARTICLE IN PRESS

Table 1. Geographical locations of the implemented gridpoints and statistical features of their SPEI-3 series

Point #	Lat.	Lon.	Elev.	mean	min	max	St. D.
1	35.75	46.25	1717	0.036	−3.450	2.610	0.983
2	35.75	46.75	2078	0.036	−3.450	2.610	0.983
3	36.25	45.75	1784	0.069	−2.609	2.404	0.967
4	36.25	46.25	1618	0.089	−2.928	2.597	0.978
5	36.25	46.75	1923	0.089	−2.928	2.597	0.978
6	36.25	47.25	1990	0.051	−2.597	3.038	0.975
7	36.75	45.75	1518	0.069	−2.609	2.404	0.967
8	36.75	46.25	1414	0.089	−2.928	2.597	0.978
9	36.75	46.75	2003	0.089	−2.928	2.597	0.978
10	36.75	47.25	2686	0.051	−2.597	3.038	0.975

ARTICLE IN PRESS

11	37.25	44.75	2598	0.028	−2.985	2.489	1.013
12	37.25	45.25	1690	0.110	−2.651	3.074	0.992
13	37.25	45.75	1268	0.110	−2.651	3.074	0.992
14	37.25	46.25	1635	0.028	−2.461	2.595	0.983
15	37.25	46.75	2012	0.028	−2.461	2.595	0.983
16	37.75	44.75	1926	0.028	−2.985	2.489	1.013
17	37.75	45.25	1278	0.110	−2.651	3.074	0.992
18	37.75	45.75	1271	0.110	−2.651	3.074	0.992
19	37.75	46.25	2699	0.028	−2.461	2.595	0.983
20	37.75	46.75	1984	0.028	−2.461	2.595	0.983
21	37.75	47.25	2187	−0.010	−2.394	3.126	0.963
22	37.75	47.75	2800	−0.010	−2.394	3.126	0.963
23	38.25	44.75	1460	0.029	−2.850	3.032	1.026
24	38.25	45.25	1268	0.015	−2.599	2.636	1.006
25	38.25	45.75	1904	0.015	−2.599	2.636	1.006
26	38.25	46.25	1505	−0.017	−2.686	2.935	0.998
27	38.25	46.75	1812	−0.017	−2.686	2.935	0.998
28	38.25	47.25	2201	0.004	−2.363	2.584	0.962
29	38.25	47.75	2792	0.004	−2.363	2.584	0.962

St. D.: Standard Deviation

ARTICLE IN PRESS

In the context of climate warming, the extremity and spatiotemporal variability in global precipitation have further intensified, while water budget processes such as earth surface evapotranspiration have undergone significant changes [36]. Flash drought manifests as a rapid decrease in soil moisture due to the combined effects of unusually high temperatures and extreme precipitation deficits, while conventional drought refers to a gradual and steady decline in soil moisture over an extended period [37]. Thus, the SPEI which considers monthly water deficit (D_i) based on both precipitation (P_i) and potential evapotranspiration (PET_i) was used in our study. It is one of the most widely used meteorological drought indices that considers the effects of P and PET in the regional climate.

$$D_i = P_i - PET_i \quad (1)$$

ARTICLE IN PRESS

It is worth noting that PET in the GDM dataset is estimated using the Thornthwaite method. The sensitivity of SPEI to alternative PET calculation approaches, such as Hargreaves–Samani or Penman–Monteith, represents an important source of uncertainty and warrants further investigation in future studies [38].

3. Methods

3.1. Proposed regional drought forecasting approach

The overall modeling process to generate RDF maps was illustrated in Figure 2. The proposed method includes four main parts: i) Data extraction and clustering analysis, ii) identifying effective *own-lags* (a variable's dependence on its past) and *cross-lags* (dependence on past values of other variables) for each centroid, iii) univariate and multivariate DL modeling (here ULNN and MLNN), and (iv) mapping SPEI at grid scale. Each of these parts and the associated methods is described in the following.

ARTICLE IN PRESS

ARTICLE IN PRESS

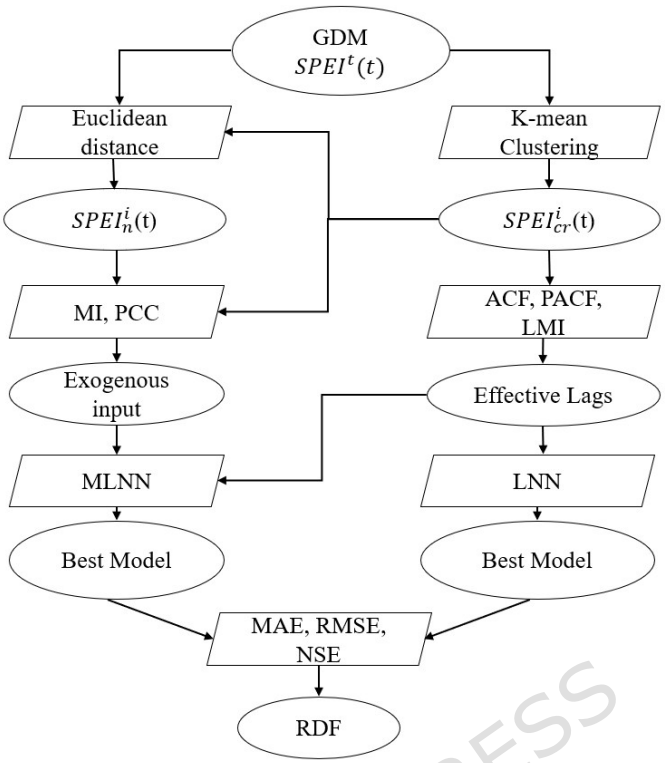


Figure 2. Flowchart illustrating the process of developing one-month ahead regional drought forecasting maps

***3.1.1**. Data extraction and clustering analysis*

Given the vast extent of input/target series at larg scale studies, employing an unsupervised clustering algorithm becomes crucial to capture the distinct kinematic patterns represented by diverse shapes of influensive varaiables [39-40]. In our case study, the dense network of grid points (here, 29 points) could potentially result in time-consuming computations and inefficiencies in modeling results across the desired region. Hence, the proposed model applies k-means clustering techniques to optimize the dimensionality of the study area via extracting homogenous SPEI regions.

ARTICLE IN PRESS

The k-means clustering is a distance-based unsupervised algorithm, widely applied for partitioning grid cells/stations into homogeneous groups based on their similarity [29,41-42]. The k-means algorithm was selected because of its computational efficiency and simplicity, which aligned with our goal of balancing model performance with scalability across a large spatial domain. However, different clustering methods can be used in future investigations depending on the purpose of studies.

The primary goal is to minimize variability within clusters while maximizing variability among clusters. The number of clusters *k* needs to be pre-defined, and each data point belongs to the cluster with the nearest centroid. The objective function, known as the squared error function (J), is given by:

$$J = \sum_{i=1}^{k} \sum_{j=1}^{n_i} \left(\left\| x_j^{(i)} - c_i \right\| \right)^2 \quad (2)$$

where k is the number of clusters, n_i is the number of data points in cluster i, $x_j^{(i)}$ is the j-th data point in cluster i, and c_i is the centroid of cluster i.

In this stage, each point's feature vector is built as shown in Eq. (3) and then, each cluster centroid is calculated using the arithmetic mean of all feature vectors belonging to that cluster (Eq. (4)).

$$x_i = [SPEI_i, Lat_i, Long_i, Elev_i] \quad (3)$$

$$c_k = \frac{1}{N_k} \sum_{i=1}^{N} x_i \quad (4)$$

ARTICLE IN PRESS

where i denotes GDM point number, k is the number of clusters, and Lat_i, $Long_i$,$Elev_i$ represent the associated points' latitude, longitude, and elevation, respectively.

By considering both SPEI vectors and geographical information, we can capture the multifaceted nature of drought and better understand its spatial variation [29]. The k-means algorithm requires prespecified the number of clusters (k) in advance. However, its optimum value is suggested to be determined via an optimization algorithm combined with the expert knowledge. Too small k values merge very different grid points into one, while too large k values create unnecessarily artificial groups. In this study, we developed a MATLAB script (see software and data availability statement) that uses *Silhouette* analysis to pick the "best" k as employed in earlier spatiotemporal prediction maodel [43]. The script guides the choice of k by balancing cluster compactness and cluster separation, ensuring that GDM points grouped truly share similar SPEI behavior and geographic attributes. The best k primarily balances regional representativeness with computational efficiency (i.e., minimizing the number of individual models required for large-scale applications). Model accuracy itself is not directly dependent on the number of clusters. However, increasing the number of clusters generally improves the spatial representation of regional drought patterns, as smaller clusters better capture local heterogeneities. Thus, a

ARTICLE IN PRESS

higher number of clusters typically enhances the overall regional fidelity of the forecasts, albeit at the cost of increased computational demand.

To attain centroid SPEI series, we simply calculated the synthetic mean SPEI series across all the GDM points in the given cluster. It's not an observed series, but characterizes the drought/wetness conditions typical of that cluster.

$$SPEI_{cr}(t) = \frac{1}{N_k}\sum_{i=1}^{N} SPEI_i(t) \quad (5)$$

Hence, $SPEI_{cr}$ is considered as the a representative profile for the entire cluster, cluster representative, and stand as the label for LNN and the benchmark model. Since the geographic features (i.e., Lat_i,$Long_i$,$Elev_i$) do not vary in time, a single value for each GDM point must be used as input for clustering. However, all inputs are normalized using *min-max* scaling to ensure that all features contribute equally to the learning process of the k-means algorithm.

ARTICLE IN PRESS

3.1.2. *Identifying effective own-and cross-lags*

To ensure univariate forecasting models capture the relevant temporal dependencies, effective own-lags are determined through investigating serial dependencies of label series using three quantitative measures: the Autocorrelation Function (ACF), the Partial Autocorrelation Function (PACF), and the Lagged Mutual Information (LMI). ACF measures the linear correlation between the cluster representative ($SPEI_{cr}(t)$) and its lagged

ARTICLE IN PRESS

series over successive monthly intervals. While the ACF measures overall correlations, it does not distinguish between direct and indirect effects of lags. The PACF resolves this issue by isolating the correlation between $SPEI_{cr}(t)$ and its lagged version while controlling for the effects of intermediate lags. Thus, the PACF complements the ACF in the model identification stage. The LMI extends beyond linear dependence by measuring both linear and nonlinear associations between the cluster representative and its lagged values [44]. It is based on information theory, quantifying the reduction in uncertainty about $SPEI_{cr}(t)$ given knowledge of the lable at lag value of m (Eq. 6).

$$LMI_{X,Y}(m) = \sum_{x\in X}\sum_{y\in Y} p(x_t, y_{t+m}) \log\left(\frac{p(x_t, y_{t+m})}{p(x_t)p(y_t)}\right) \quad (6)$$

In case of multivariate time series models, exogenous features (covariates) and their lags could be also considered to increase models accuracy. Exogenous variables are predictors that are independent of the model being used for forecasting, and their future values must be known in order to include them in the prediction process. In this study, the exogenous inputs were identified among the GDM points that are closest (i.e., minimum Euclidean distance) to each cluster centroid in the geographic space (latitude–longitude–elevation) and the feature space (SPEI time series). Once exogenous inputs are selected, we identified the most informative lags of exogenous features via their linear or nonlinear dependencies with $SPEI_{cr}(t)$ using Pearson Correlation Coefficient (PCC) and Mutual Information (MI)

ARTICLE IN PRESS

tools. While the PCC captures only the linear relationship between two series, the MI measures how much knowing one variable reduces uncertainty about another.

$$MI_{X,Y} = \sum_{x \in X} \sum_{y \in Y} p(x_t, y_t) \log \left(\frac{p(x_t, y_t)}{p(x_t) p(y_t)} \right) \quad (7)$$

Previous studies have shown that the joint probability of labels and associated features in Eqs. (6,7) can be estimated via histogram binning method [44-45]. Therefore, MI and LMI values will depend on how the histograms are constructed, i.e., the width and number of the bins. In this study, first, the square-root rule was used to determine approximate number of bins and then we computed MI with slightly different number bins (here 10 to 50 by steps of five) to ensure results are robust. Since MI and LMI depend on the probability distributions, range from 0 to +∞ while ACI, PACF, and PCC range between -1 and +1.

ARTICLE IN PRESS

3.1.3 State-of-the-art LNN

The LNNs, a.k.a Liquid Time-Constant Networks [46], present a novel paradigm in DL, offering a new generation of recurrent neural networks (RNNs). The key innovation over earlier DLs is that its parameters (the "weights" that define its calculations) are not static. Instead, they change dynamically based on the input they receive, much like a fluid adjusts its shape and flow in response to forces acting upon it. The RNNs, determined by ordinary differential equations (ODEs), can continue adapting to new stimuli after training, demonstrating strong performances in time series

ARTICLE IN PRESS

prediction [47-49]. The state of a neural ODE is defined by the solution of this equation:

$$\frac{dx(t)}{dt} = f(x(t), I(t), t, \theta) \quad (8)$$

where $f(.)$ is a neural network parametrized by θ, $x(t)$ denotes the hidden state, $I(t)$ is the input vectors, and t represents time.

The LNN determines the derivatives of $x(t)$ through a stable continuous-time RNN instead of a direct neural network solver. To this end, an improved ordinary differential equation (Eq. 9) was proposed [50] (Hasani et al. 2018).

$$\frac{dx(t)}{dt} = -\frac{x(t)}{\tau} + f(x(t), I(t), t, \theta) \quad (9)$$

where the term of $-\frac{x(t)}{\tau}$ is designed to assist the system to reach an equilibrium state with a time-constant τ. This model can be alternatively rewritten as follows:

$$\frac{dx(t)}{dt} = -\frac{x(t)}{\tau} + S(t) \quad (10)$$

where $S(t)$ nonlinear synapse representing dynamics of exogenous input $I(t)$, recurrent inputs from hidden states $x(t)$, nonlinear transmission of neurotransmitters, the probability of activation of receptors and the concentration of available neurotransmitters.

$$S(t) = f(x(t), I(t), t, \theta)(A - x(t)) \quad (11)$$

where A is the bias component of the neural network.

ARTICLE IN PRESS

By combining Eq. (10) and Eq. (11), the ODE for LNNs can be expressed as Eq. (12). Therefore, the hidden state of an LNN is determined by the solution of this initial value problem.

$$\frac{dx(t)}{dt} = -\left[\frac{1}{\tau} + f(x(t), I(t), t, \theta)\right]x(t) + f(x(t), I(t), t, \theta)(A) \quad (12)$$

To solve this *ODE,* Hasani et al. [46] fuses the implicit and explicit Euler methods in which hidden states at next time step $x(t + \Delta t)$ *can be obtained sequentially .*

$$x(t + \Delta t) = \frac{x(t) + \Delta t f(x(t), I(t), t, \theta)A}{1 + \Delta t(\omega + f(x(t), I(t), t, \theta)} \quad (13)$$

where $\omega = \frac{1}{\tau}$.

3.1.4 *Mapping regional SPEI forecasts*

Using the best five attained LNN models, one-month ahead SPEI-3 forecasting map is generated by applying the forecasts to the corresponding GDM points within each cluster. The map shows both numerical SPEI-3 values and drought categories, which classified wet/dry conditions into five levels (Table 4) based on the SPEI thresholds as suggested by Danandeh Mehr et al. [51]. The forecasting maps are compared with observed SPEI-3 values to assess model's performance to capture spatial variability of drought across the LUB.

Table 2. Classifications of wet and dry conditions base on SPEI indices

Classification	SPEI threshold
Wet	SPEI ≥ 1.00
Near normal (NN)	−1.00 ≤ SPEI <1.00
Moderate drought (MD)	−1.42≤SPEI < −1.00

ARTICLE IN PRESS

Severe drought (SD)	−1.83 <SPEI < −1.42
Extreme drought (ED)	SPEI ≤ −1.83

3.2. Baseline model

In the present of seasonality, which is the case in SPEI series, Seasonal AutoRegressive Integrated Moving Average (SARIMA) is one of the most famous and widely used univariate time series modeling in in fields like hydrology [52-54]. The method can capture autocorrelation in the data through autoregressive and moving average terms and handle non-stationarity and seasonality, through integrating and Seasonal terms, respectively. The model is commonly expressed as SARIMA$(p,d,q)(P,D,Q)_m$ in which p, d, and q are non-seasonal components; P, D, and Q are the seasonal backshifts and the letter m denotes the number of samples in a year (e.g., m=12 for monthly data). Equation (14) expresses an example of a first-order SARIMA model without a constant for a set of quarterly data (i.e., $m = 4$) [54].

$$\text{SARIMA}\ (1,1,1)(1,1,1)_4: (1 - \phi_1 B)\ (1 - \Phi_1 B^4)(1 - B)(1 - B^4)yt = (1 + \theta_1 B)\ (1 + \Theta_1 B^4)\varepsilon_t \quad (14)$$

where ϕ_1 and θ_1 are the parameters of non-seasonal and Φ_1 and Θ_1 are the parameters of seasonal components of the model. The term ε_t is white noise.

It is seen that the additional seasonal terms are simply multiplied by the non-seasonal terms. Like ARIMA modeling, the seasonal backshift parameters (Φ and Θ) can be determined through either a correlogram analysis or from an analytical stationarity test such as Augmented Dickey-Fuller (ADF). In this

ARTICLE IN PRESS

study, ADF was used to check stationarity, and differencing was applied for the SPEI series if needed. For optimal model selection, mulltiple SARIMA configurations were tested and the model with lowest Akaike Information Criterion (AIC) was choosed. For more details about parameter tuning in SARIMA, the interested reader is referred to Bender and Simonovic (1994).

3.3 Performance evaluation

Four performance evaluation criteria, including Nash-Sutcliffe efficiency (NSE), mean-square error (MSE), root-mean-square error (RMSE), and mean absolute error (MAE), were usd in this study. Note that the NSE ranges from $-\infty$ to 1, where an NSE of 1 indicates a perfect match between the predicted and observed SPEI, while RMSE decrease as model accuracy increases.

$$NSE = 1 - \frac{\sum\left(SPEI_{f_i} - SPEI_{o_i}\right)^2}{\sum\left(SPEI_{o_i} - \overline{SPEI_o}\right)^2} \quad (15)$$

$$RMSE = \sqrt{\frac{\sum\left(SPEI_{f_i} - SPEI_{o_i}\right)^2}{n}} \quad (16)$$

$$MSE = \frac{\sum\left(SPEI_{f_i} - SPEI_{o_i}\right)^2}{n} \quad (17)$$

$$MAE = \frac{\sum\left|SPEI_{f_i} - SPEI_{o_i}\right|}{n} \quad (18)$$

ARTICLE IN PRESS

where n is the number of samples, $SPEI_{f_i}$ is the forecasted value, and $SPEI_{o_i}$ is the observed value. These are well-known indices that were also used for intercomparision between different DL models [55-57].

4. Results and discussion

4.1. Clustering results

The proposed k-means clustering algorithm, combined with Silhouette criterion, classified the GDM points into five clusters (Figure 3b), considering SPEI-3, latitude, longitude, and elevation as features. To avoid creating unnecessarily artificial clusters, the Silhouette analysis was performed for k values two to nine (Figure 3a). The average Silhouette score implies that for k=5, each GDM point fits well within its cluster compared to other clusters. Figure 3b also shows the position of centroids that reflect the averages of the coordinates of the associated GDM points.

ARTICLE IN PRESS

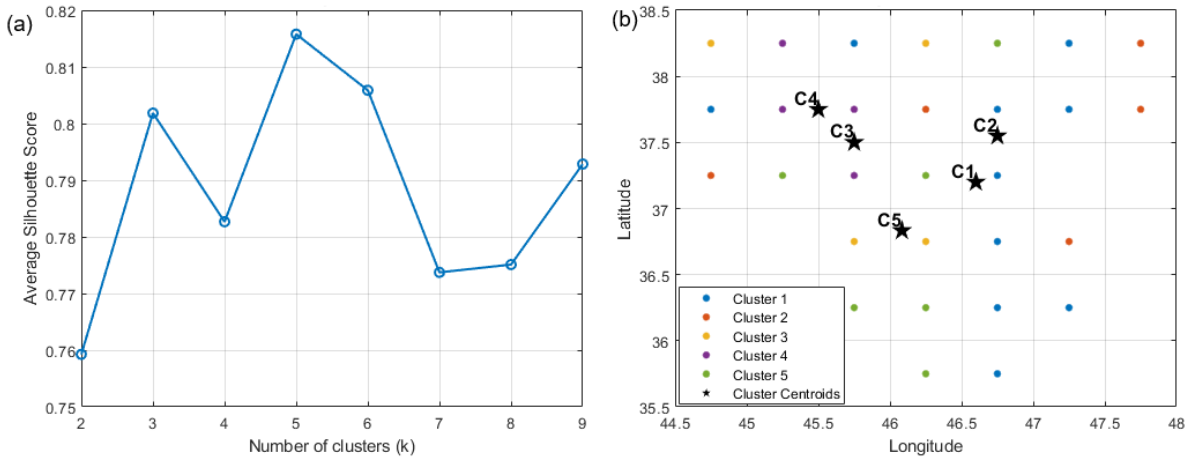


Figure 3. The (a) average Silhouette score attained for clustering 29 GDM points, and (b) five centroids positions across the study area

ARTICLE IN PRESS

To demonstrate the spatial variability of meteorological drought patterns within the LUB boundaries, the clustering results were transferred to the Google Earth Pro Tool (Figure 4). The figure shows that approximately the entire Lake Urmia is located in a single cluster, which makes sense physically. Tabriz and Urmia, the capital cities of East and West Azarbaijan provinces, showed dissimilar drought patterns. This agrees with the strong consensus in the scientific literature that changes in land cover, primarily the massive expansion of irrigated agriculture, are the dominant driver of drought and desiccation of Lake Urmia [58-59].

The monthly SPEI-3 values were calculated for five centroids, serving as the representative regional meteorological drought signals during both the training and testing phases (Figure 5). Therefore, instead of monitoring and modeling 29 individual series, the cluster-centroid SPEI (i.e., $SPEI_{cr}(t)$) will be forecasted as a proxy for the cluster. It is worth noting that the proposed algorithm does not re-calculate SPEI. It averages the already loaded SPEI time series of GDM points within each cluster to form a centroid series. Thus, the obtained centroid series is the mean drought history of that cluster as formulated in Eq. (5).

ARTICLE IN PRESS

ARTICLE IN PRESS

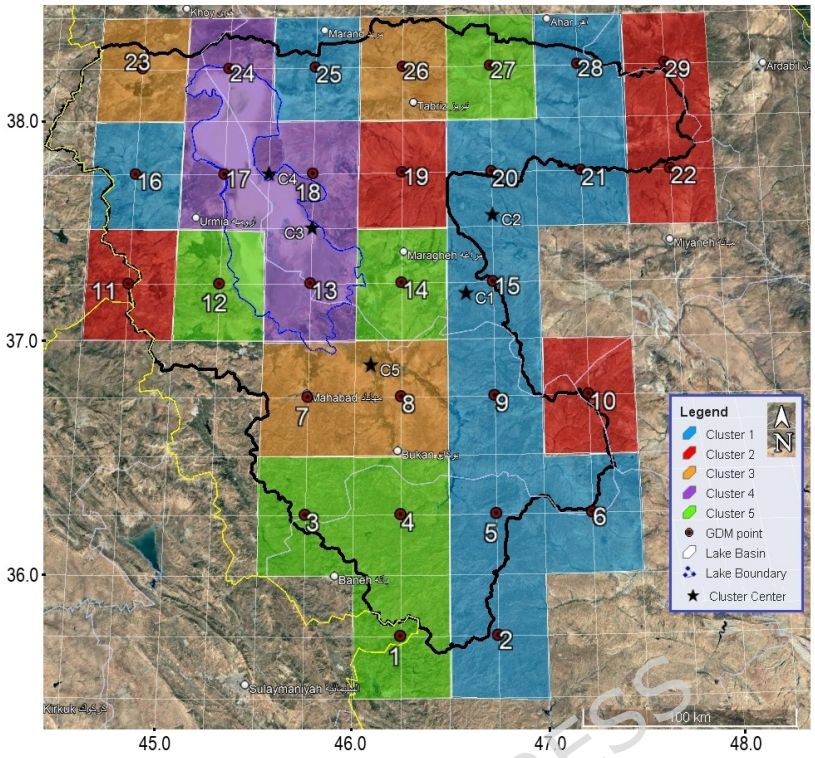


Figure 4. Cluster map, considering SPEI-3, latitude, longitude, and elevation within the Lake Urmia Basin. The numbering on the black asterisks represents corresponding cluster number (The map was generated using Google Earth Pro_7.3.71155).

.

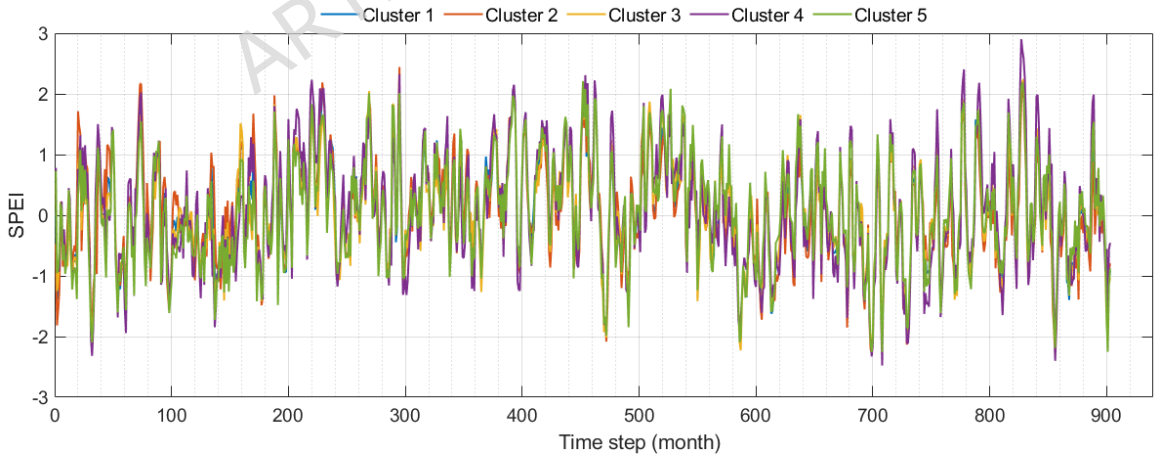


Figure 5. Cluster representative SPEI-3 series ($SPEI_{cr}$) for five centroids .

4.1.1. 2D and 3D assessment of spatial distribution of clusters

To assess the spatial variation of the regional drought pattern, two-dimensional (2D) and three-dimensional (3D) plots of cluster distributions versus geographic features were depicted in Figures 6 and 7, respectively.

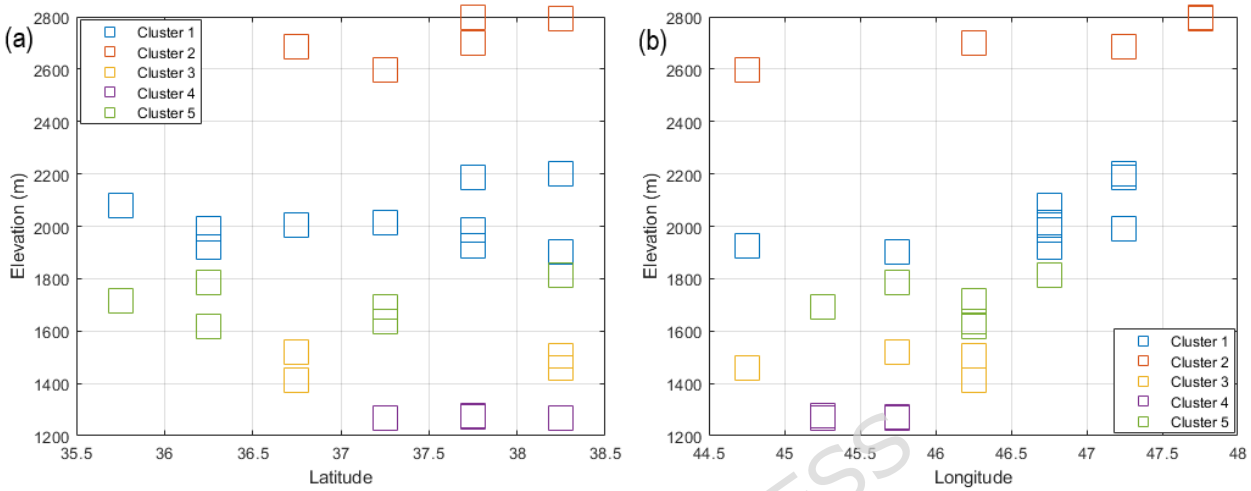


Figure 6. Cluster separation by (a) latitude/elevation and (b) longitude/elevation within the Lake Urmia Basin.

Figure 6 shows a strong correlation between location/elevation and clusters. It effectively demonstrates that the drought pattern across the LUB is not random and systematically organized by fundamental geographic factors—primarily elevation which may modify local precipitation patterns. It is observed that the GDM points which are geographically close and at similar elevations tend to have similar SPEI patterns. Such a clear separation between clusters confirms that the choice of five clusters (k=5) was effective. This result is consistent with the findings of Ghorbani-Aghdam et al. [60], who identified five homogeneous drought regions within the LUB by applying factor analysis to historical 3-month SPI time series.

ARTICLE IN PRESS

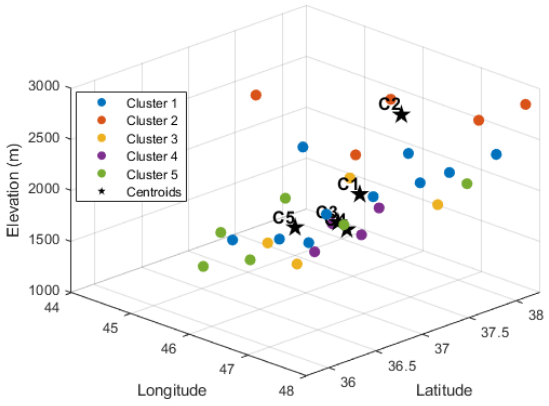


Figure 7. The 3D plot of spatial distribution of clusters and associated centroids across the Lake Urmia Basin.

In Figure 7, the position of the centroids reveals the defining geographic and topographic niche that governs the drought pattern for each cluster. The most dramatic variation between centroids is along the Z-axis (Elevation). Centroid position of Cluster #2 represents high-latitude, high-altitude GDM points. This is the signature of major mountain ranges in temperate regions where drought pattern may be heavily influenced by orographic precipitation. The centroid's high latitude also suggests a cooler climate with seasonal variability driven by mid-latitude cyclones. Clusters #4 and #5 are sharply separated from Clusters #1, #2, and #3 based primarily on elevation. This overwhelmingly confirms that topography is the dominant factor controlling meteorologically homogeneous regions across LUB. Our findings is consistent with those of Fazel et al. [61] in which the authors demonstrated that the spatial distribution of precipitation pattern across LUB mostly follows the topography of the region and lessly affected by local atmospheric circulation.

ARTICLE IN PRESS

4.2. Feature selection results

As previously mentioned, ACF, PACF, and LMI (Figure 8) analysis were applied on each cluster representative SPEI-3 series ($SPEI_{cr}(t)$) to select the top-ranked own-lags. Seasonal spikes in the ACF diagrams indicate annual cycles in the data. Therefore, the SARIMA is considered the standard univariate benchmark model. The PACF diagrams also show a higher non-isolating correlation between $SPEI_{cr}(t)$ and its 4^{th} lag. The LMI values show that stronger dependency (linear or nonlinear) only exists in the first two month lags. Therefore, one-month-ahead regional SARIMA and ULNN models for all clusters are formulated as follows.

$$SPEI^{i}_{cr}(t) = f(SPEI^{i}_{cr}(t-1), SPEI^{i}_{cr}(t-2), SPEI^{i}_{cr}(t-3), SPEI^{i}_{cr}(t-4), SPEI^{i}_{cr}(t-12), SPEI^{i}_{cr}(t-25)) \quad (19)$$

where superscript *i* represent the centroid ID.

ARTICLE IN PRESS

ARTICLE IN PRESS

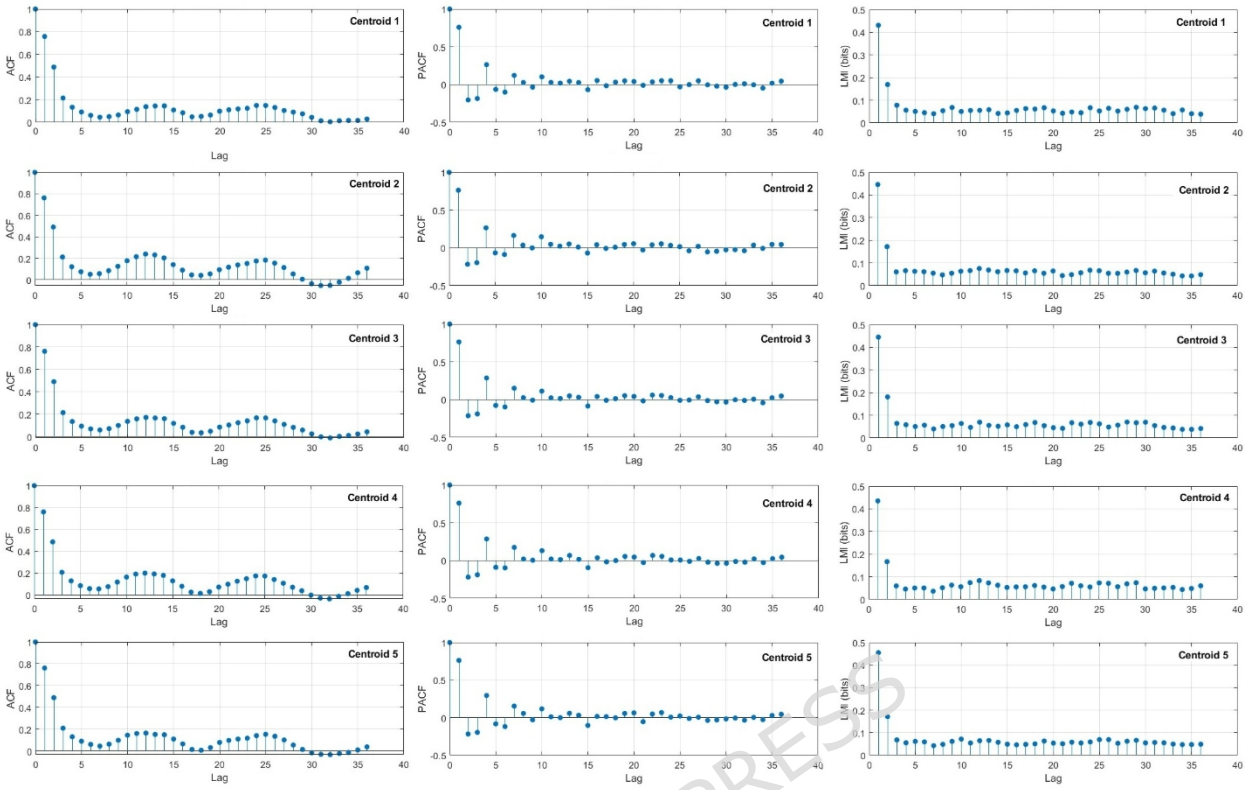


Figure 8. ACF, PACF, and LMI diagrams depicted for centroid representative SPEI series

To develop multivariate forecasting models, the exogenous inputs were identified among the GDM points regarding their Euclidean distance to each cluster centroid. Table 3 sumarizes geographical locations of the centroids and the nearest points (i.e., exogenous features) for each cluster. The results showed that both geographical- and feature-based approaches resulted in identical exogenous inputs. Therefore, the effective lags of GDM points 15, 19, 23, 18, and 1 are determined via PCC and MI analysis (see Figure 9) as the external inputs for the clusters #1 to #5, respectively.

Table 3. Geographical features of the centriods, associated GDM gridpoints, and the nearest point (exogenoius feature position) to the centriod

ARTICLE IN PRESS

ter	GDM Point ID	Centroid			Geographic nearest point					Feature-based nearest point				
		Lat.	Lon.	Elev. (m)	Point ID	Lat.	Lon.	Elev. (m)	Distance	Point ID	Lat.	Lon.	Elev. (m)	Dista
	2,5,6,9,15,16, 20,21,25,28	37.2	46.60	2021	15	37.25	46.75	2012	8.8014	15	37.25	46.75	2012	13.1
	10,11,19,22,29	37.55	46.75	2715	19	37.75	46.25	2699	16.0090	19	37.75	46.25	2699	19.1
	7,8,23,26	37.5	45.75	1474	23	38.25	44.75	1460	14.3047	23	38.25	44.75	1460	21.2
	13,17,18,24	37.75	45.50	1271	18	37.75	45.75	1271	0.35355	18	37.75	45.75	1271	4.82
	1,3,4,12,14,27	36.83	46.08	1709	1	35.75	46.25	1717	7.74462	1	35.75	46.25	1717	18.5

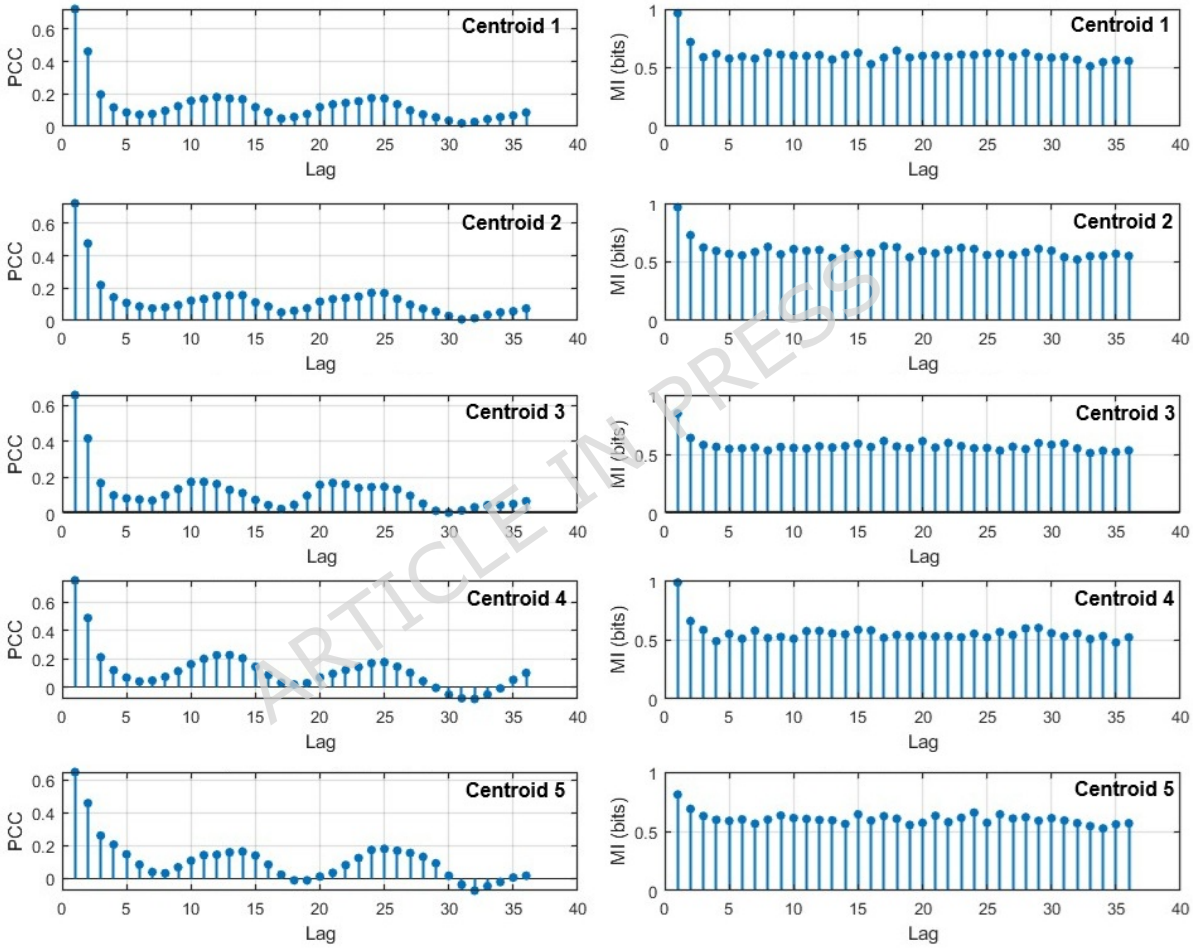


Figure 9. PCC and MI diagrams attained for centroid representative SPEI series and associated exogenous features

According to Figure 9, the 1st, 2nd, 12th, and 24th lags of the exogenous inputs were selected as the external inputs for the models. Therefore, a one-month-ahead MLNN forecasting model can be formulated as follows.

ARTICLE IN PRESS

$$SPEI^{i}_{cr}(t) = f(SPEI^{i}_{cr}(t-1), SPEI^{i}_{cr}(t-2), SPEI^{i}_{cr}(t-3), SPEI^{i}_{cr}(t-4), SPEI^{i}_{cr}(t-12), SPEI^{i}_{cr}(t-25), SPEI^{x}_{cr}(t-1), SPEI^{x}_{cr}(t-2), SPEI^{x}_{cr}(t-3), SPEI^{x}_{cr}(t-12)) \quad (20)$$

Among these lags, the 12-month lag aligns with annual climate cycles (e.g., ENSO influences) and shows strong dependency in all ACF, PACF, LMI, PCC, and MI plots. This lag has also been selected as an effective input for SPI and SPEI forecasting in various regions of Iran [14].

4.3 Modeling results for five centroids

4.3.1. SARIMA Results

ARTICLE IN PRESS

For each centroid, we used MATLAB software to fit several one-step-ahead recursive SARIMA models. The best models' orders were selected based on a small grid search over (p, q) and seasonal (P, Q) parameters using the AIC. Table 4 summarizes the performance of the attained models for one-month-ahead SPEI-3 forecasting during the training and testing periods across five centroids. It is worth noting that the current "forecast" function in MATLAB generates multiple steps ahead without refitting, which is also known as a static multi-step forecast, where the model is not updated with new observations. Thus, for a true one-step-ahead forecast (refitting at each step), we developed a new script and implemented a loop that updates the model with each new observation (see software and data availability statement). Thus, the model uses the first 80% of data, indicated by the vertical dashed line in Figure 10, for static training and then dynamically forecasts the next

ARTICLE IN PRESS

20% (with 180 samples spanned from May 2010 to April 2025) with updating. Indeed, for each step in the test set, we update the model with the new observation and then forecast the next step. This is more computationally intensive but more accurate. Figure 10 depicted actual and SARIMA fitted/forecasted SPEI series at each centroid. SARIMA forecasts at Centroid #4 were also magnified to show model fluctuations and confidence intervals (CI) clearly. The baseline SARIMA models' accuracy remains below 50% in terms of NSE, which proves the complexity of the SPEI-3 series and the requirement for more robust ML/DL models. However, the positive values imply that the model is more accurate than the mean of the observed data. It shows a slight improvement on the test set for almost all clusters. This is unusual but suggests no overfitting.

Table 4. Performance of the univariate SARIMA models for one-month-ahead SPEI-3 forecasting during the training and testing period across five centroids.

			Train				Test			
Cluster ID	**Model Orders**	**AIC**	**MSE**	**RMSE**	**MAE**	**NSE**	**MSE**	**RMSE**	**MAE**	**NSE**
1	(2,0,2)(1,0,1)12	1563.2	0.500	0.707	0.551	0.293	0.477	0.691	0.522	0.342
2	(1,0,1)(2,0,2)12	1642.8	0.559	0.748	0.574	0.239	0.519	0.720	0.553	0.248
3	(1,0,1)(2,0,2)12	1591.6	0.521	0.721	0.558	0.241	0.494	0.703	0.545	0.378
4	(2,0,2)(1,0,1)12	1707.2	0.611	0.781	0.601	0.293	0.610	0.781	0.617	0.454
5	(2,0,2)(1,0,1)12	1621.0	0.542	0.736	0.563	0.264	0.524	0.724	0.550	0.305

ARTICLE IN PRESS

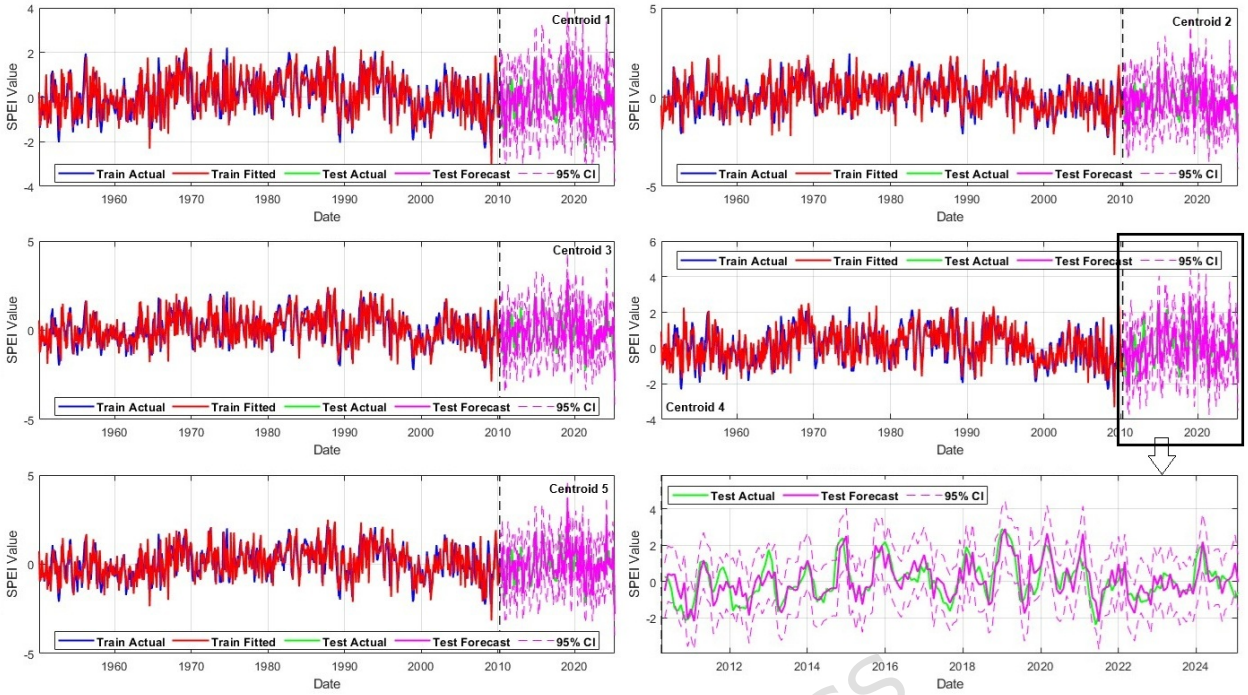


Figure 10. Time series plots of centroid representative SPEI-3 series and associated SARIMA forecasts

ARTICLE IN PRESS

4.3.2. LNN Results

Currently, MATLAB doesn't have a built-in "liquid neural network" tool. Thus, we first developed a new MATLAB script and then applied it to each centroid. To this end, a custom LiquidLayer (a recurrent layer with learnable time constants) was coded. The layer takes input features and transfers them to a fully connected layer before moving to the regression layer (see software and data availability statement). Similar to SARIMA runs, the script splits the inputs into training (80%) and testing (20%) sets, trains and evaluates the models, and plots LNN forecasts against the target SPEIcr series. The primary hyperparameter specific to the LNN architecture, the number of liquid neurons, was set to 16. This choice was informed by the inherent efficiency of LNNs, which achieve high expressivity and strong performance

ARTICLE IN PRESS

in time-series tasks with significantly fewer neurons compared to traditional recurrent architectures (e.g., LSTM or GRU) [62]. Previous studies on LNNs and related continuous-time models have demonstrated effective modeling of complex sequential dynamics using small networks (often in the range of 10–20 neurons), balancing computational efficiency, stability, and generalization while avoiding overfitting on our regional-scale SPEI dataset. The training hyperparameters (Adam optimizer, Max Epochs=100, Mini Batch Size=32, Initial Learn Rate=0.01) were selected based on common best practices for training recurrent and time-series forecasting networks in MATLAB. The Adam optimizer is widely recommended for its adaptive learning rates and robust convergence in hydrological and drought modeling applications. The learning rate of 0.01, batch size of 32, and epoch limit of 100 represent standard starting values that provided stable training progress without early divergence, as monitored through validation performance (with early stopping implicitly guided by no further improvement). Optimal models were selected through a trial-and-error process (10 repetitions per architecture) based on minimum RMSE, which penalizes larger errors more heavily. Table 5 presents the performance of the best ULNN and MLNN models for one-month-ahead SPEI-3 forecasting across five centroids. Figures 11 and 12 illustrate the LNN fitted values and forecasts, respectively.

Table 5. Performance of the LNN models developed for 1-month-ahead forecasting during the training and testing periods across five centroids

Model	Cluster ID	Train				Test			
		MSE	RMSE	MAE	NSE	MSE	RMSE	MAE	NSE
	1	0.241	0.491	0.376	0.660	0.477	0.514	0.379	0.639

ARTICLE IN PRESS

ULNN (Eq. 10)	2	0.259	0.509	0.390	0.645	0.275	0.525	0.389	0.603
	3	0.235	0.485	0.370	0.657	0.272	0.521	0.392	0.663
	4	0.301	0.549	0.425	0.654	0.365	0.604	0.456	0.677
	5	0.253	0.503	0.389	0.656	0.270	0.519	0.386	0.647
MLNN (Eq. 11)	1	0.053	0.231	0.182	0.925	0.034	0.186	0.142	0.953
	2	0.059	0.243	0.190	0.919	0.039	0.198	0.153	0.944
	3	0.096	0.310	0.245	0.860	0.119	0.344	0.275	0.853
	4	0.017	0.130	0.103	0.980	0.023	0.152	0.124	0.979
	5	0.116	0.340	0.267	0.843	0.156	0.395	0.309	0.796

ARTICLE IN PRESS

ARTICLE IN PRESS

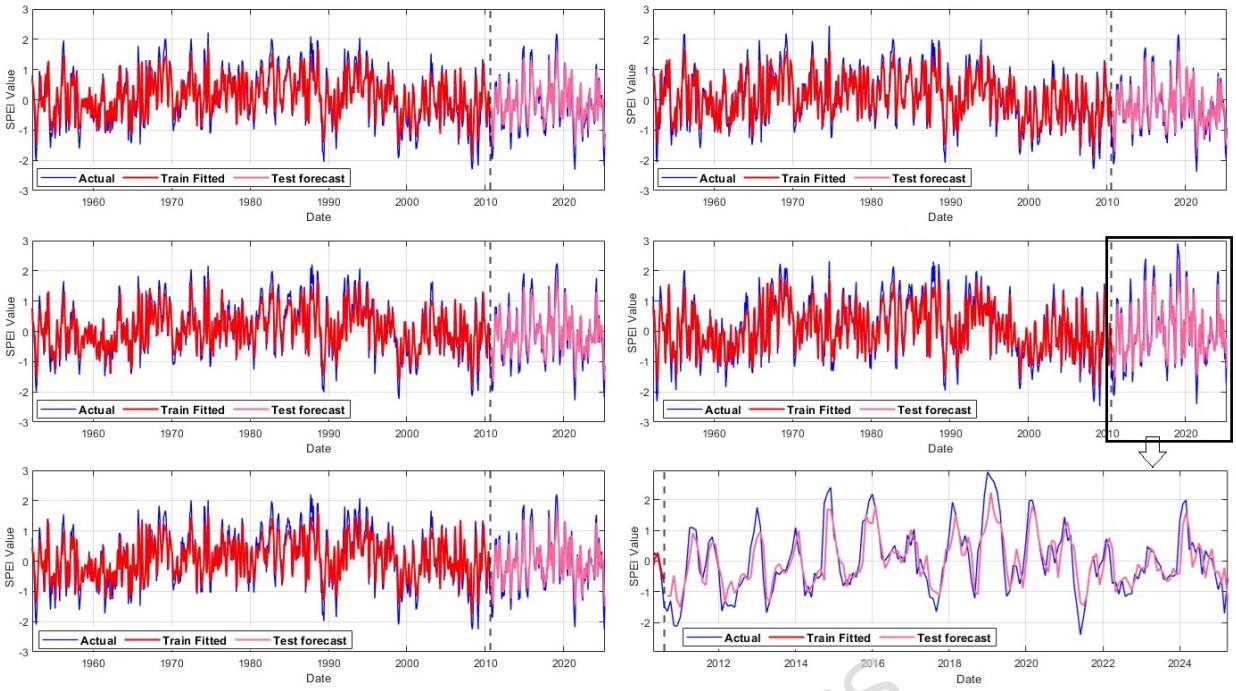


Figure 11. Time series plots of centroid representative SPEI series and associated univariate LNN forecasts

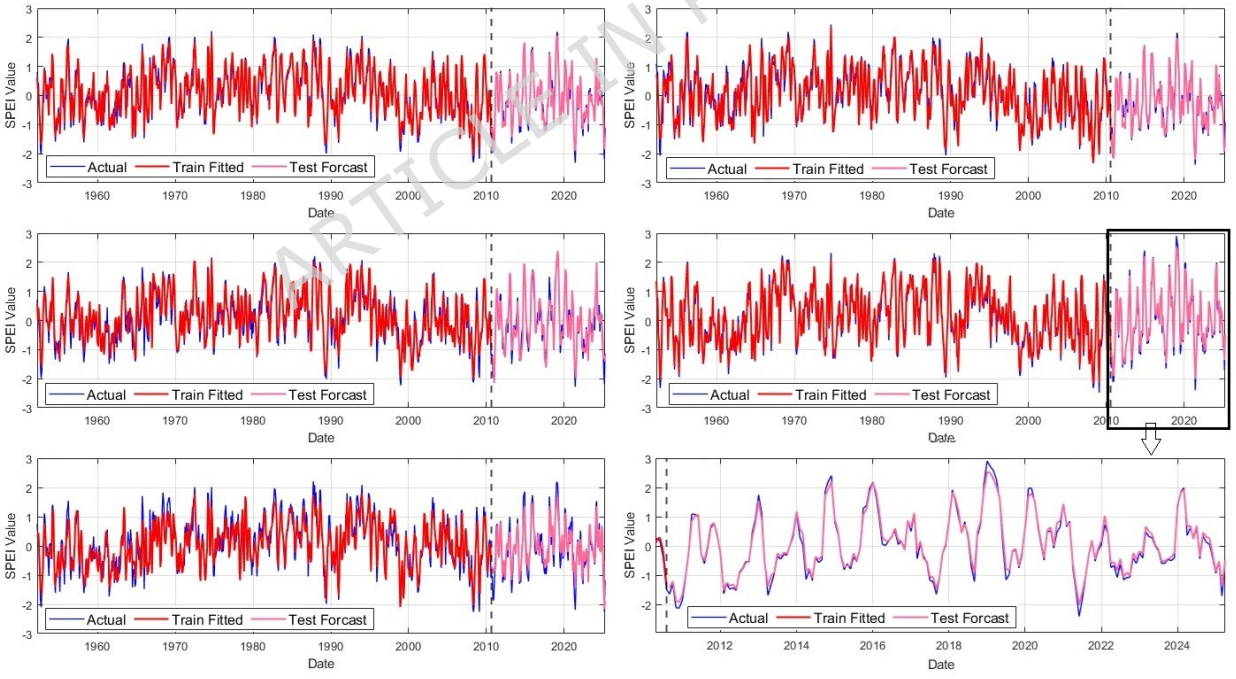


Figure 12. Time series plots of centroid representative SPEI series and associated multivariate LNN forecasts

ARTICLE IN PRESS

The table indicates that the MLNN approach consistently yields higher accuracy than ULNN in all clusters. The NSE values exceeded 0.8 for all five centroids, with a maximum NSE of 0.979, and minimum RMSE values of 0.124 at Cluster #4. Notably, this centroid almost represents the GDM points that are within or in the proximity of the lake extent, characterized by lower elevations across the LUB. A key sign of a robust model is a minimal difference between its performance on the training and test sets. The MLNN shows almost identical performance between the training and test sets (e.g., Test NSE = 0.979 vs. Train NSE = 0.980 at cluster #4). This is an ideal scenario, and indicates that MLNN generalizes perfectly. It has learned the underlying pattern in the data without memorizing the noise.

ARTICLE IN PRESS

4.3.3. Inter-model comparison

As detailed in Table 6, the three models are compared quantitatively based on regional averages of key accuracy metrics. The results demonstrate a substantial performance gain from the SARIMA to the ULNN model, followed by a further significant leap from the ULNN to the MLNN architecture.

Table 6. Mean regional performance of the models during training and testing.

	Train				Test			
Model	**MSE**	**RMSE**	**MAE**	**NSE**	**MSE**	**RMSE**	**MAE**	**NSE**
SARIMA	0.547	0.739	0.569	0.266	0.525	0.724	0.557	0.345
ULNN	0.258	0.507	0.390	0.654	0.332	0.537	0.400	0.646
MLNN	0.068	0.251	0.197	0.905	0.074	0.255	0.201	0.905

ARTICLE IN PRESS

Comparing SARIMA with the ULNN model, the test MSE and MAE dropped by 36.8% (from 0.525 to 0.332) and 28.2% (from 0.557 to 0.400), respectively. The NSE score more than doubled from 0.345 to 0.646, a huge improvement. Another massive leap is seen when comparing the MLNN model with ULNN. While the test MSE and MAE were cut by 77.7% (from 0.332 to 0.074) and 49.8% (from 0.400 to 0.201), respectively, the test RMSE was nearly halved (from 0.537 to 0.255). The NSE score increased to 0.905, which means the model performance improved to an "excellent" level. Therefore, exhibiting the average prediction error less than half that of the baseline SARIMA model, MLNN is unequivocally the best model, demonstrating superior accuracy and, crucially, excellent generalization with virtually no gap between its training and test performance.

ARTICLE IN PRESS

Additionally, we investigated the impact of physical attributes on model accuracy by plotting performance against centroid elevations in Figure 13. The results reveal that all models achieved higher accuracy at lower elevations, particularly at the lake surface. Univariate models (SARIMA and ULNN) exhibited a clear decline in accuracy with increasing elevation, whereas the MLNN showed no consistent downward trend. This decreasing accuracy in univariate models may stem from the influence of additional hydrologic variables on SPEI variability at higher elevations. These findings underscore the advantage of incorporating exogenous features into the LNN

ARTICLE IN PRESS

(i.e., $SPEI_{cr}^{x}$ and its effective lags) for improved performance across varied topographies.

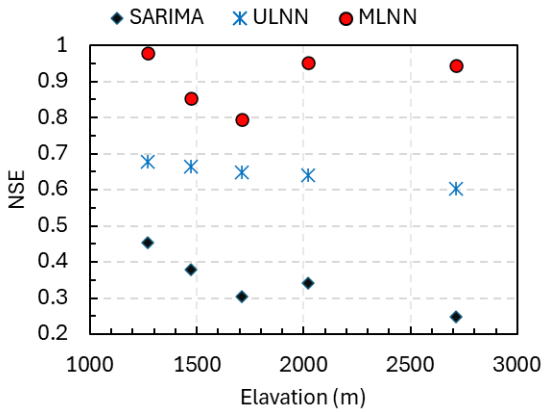


Figure 13. The relationship between model accuracy and elevation

The distinction between lowlands and highlands underscores the need for spatially adaptive modeling approaches that account for the diverse roles of environmental factors across different climatic contexts. Many large-scale drought prediction studies, such as Madadgar et al. [7] and Dikshit et al. [63], often overlook the influence of topographic conditions. To enhance the accuracy and effectiveness of drought prediction models and maps, it is critical to tailor them to both topographic variations and regional feature space characteristics, thereby addressing localized drought challenges more effectively.

ARTICLE IN PRESS

4.4. RDF maps

The RDF maps across the LUB were generated by applying MLNN forecasts from five centroids to their corresponding GDM points. Table 7 evaluates the

ARTICLE IN PRESS

spatial performance of the proposed model for SPEI-3 forecasting across 29 GDM points in the LUB, using RMSE, NSE, and total classification accuracy (TA; percentage of grid cells correctly classified into drought severity categories).

Table 7. Spatial performance of the proposed MLNN model across LUB

Point ID	Train			Test			Point ID	Train			Test		
	RMSE	NSE	TA	RMSE	NSE	TA		RMSE	NSE	TA	RMSE	NSE	TA
1	0.46	0.79	75.61	0.49	0.72	81.25	16	0.60	0.63	75.61	0.68	0.62	68.75
2	0.68	0.53	68.76	0.60	0.57	78.41	17	0.12	0.99	91.73	0.15	0.98	93.18
3	0.54	0.71	73.18	0.43	0.74	83.52	18	0.12	0.99	91.73	0.15	0.98	93.18
4	0.48	0.77	76.46	0.53	0.68	80.11	19	0.25	0.93	86.31	0.22	0.95	85.23
5	0.54	0.70	73.61	0.50	0.71	84.66	20	0.27	0.92	83.45	0.26	0.93	81.82
6	0.57	0.67	75.32	0.44	0.76	78.98	21	0.54	0.69	75.46	0.47	0.63	76.70
7	0.69	0.52	70.33	0.57	0.55	76.70	22	0.48	0.75	78.32	0.42	0.71	78.41
8	0.64	0.59	72.33	0.61	0.57	77.27	23	0.41	0.82	83.45	0.44	0.87	75.57
9	0.54	0.70	73.61	0.50	0.71	84.66	24	0.56	0.66	74.32	0.63	0.67	68.18
10	0.58	0.65	73.18	0.49	0.71	78.98	25	0.57	0.65	73.89	0.56	0.74	72.73
11	0.61	0.62	74.18	0.69	0.63	67.05	26	0.58	0.64	76.03	0.67	0.52	68.18
12	0.57	0.66	73.89	0.69	0.59	73.86	27	0.68	0.51	73.04	0.65	0.55	69.32
13	0.12	0.99	91.73	0.15	0.98	93.18	28	0.67	0.51	70.47	0.50	0.64	72.16
14	0.60	0.62	73.04	0.60	0.62	74.43	29	0.62	0.59	72.33	0.44	0.71	73.30
15	0.27	0.92	83.45	0.26	0.93	81.82	-	-	-	-	-	-	

During the testing period, NSE values range from 0.52 to 0.98 with an average of approximately 0.72, while TA ranges from 67.05% to 93.18% with an average of around 78%. The model exhibits strong performance at several points, achieving NSE ≥ 0.90 and TA ≥ 85% at points such as 13, 17, 18, and 19, indicating excellent capture of drought dynamics in those clusters. In

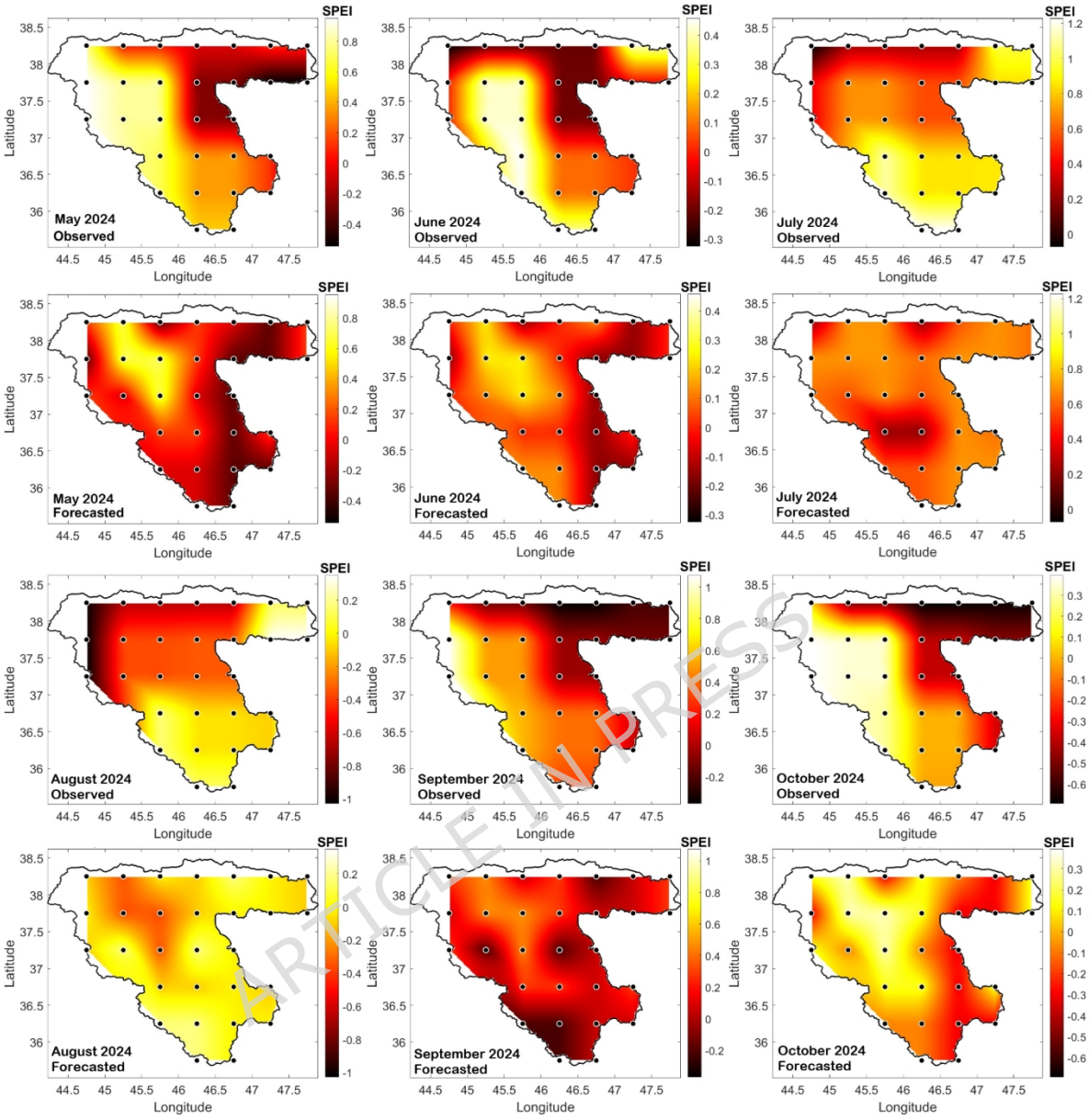
ARTICLE IN PRESS

contrast, lower performance is observed at points like 11, 26, and 27 (NSE ≈ 0.52–0.63, TA ≈ 67–69%), suggesting moderate challenges in reproducing SPEI variability in certain sub-regions. Overall, the majority of points show satisfactory to good performance (NSE > 0.60 and TA > 70%), with testing metrics generally comparable to or slightly lower than training, demonstrating reasonable generalization and acceptable spatial accuracy for a regional-scale drought forecasting model. These values are consistent with acceptable performance levels reported in the literature for RDF models [24].

As an example, RDF maps depicted for the last year of the testing period (May 2024 to April 2025) were compared numerically in Figure 14 and categorically in Figure 15. While the generated maps provided generally skillful forecasts and effectively captured the spatial variability of drought conditions, their quantitative performance was also evaluated in Table 8.

ARTICLE IN PRESS

ARTICLE IN PRESS



ARTICLE IN PRESS

ARTICLE IN PRESS

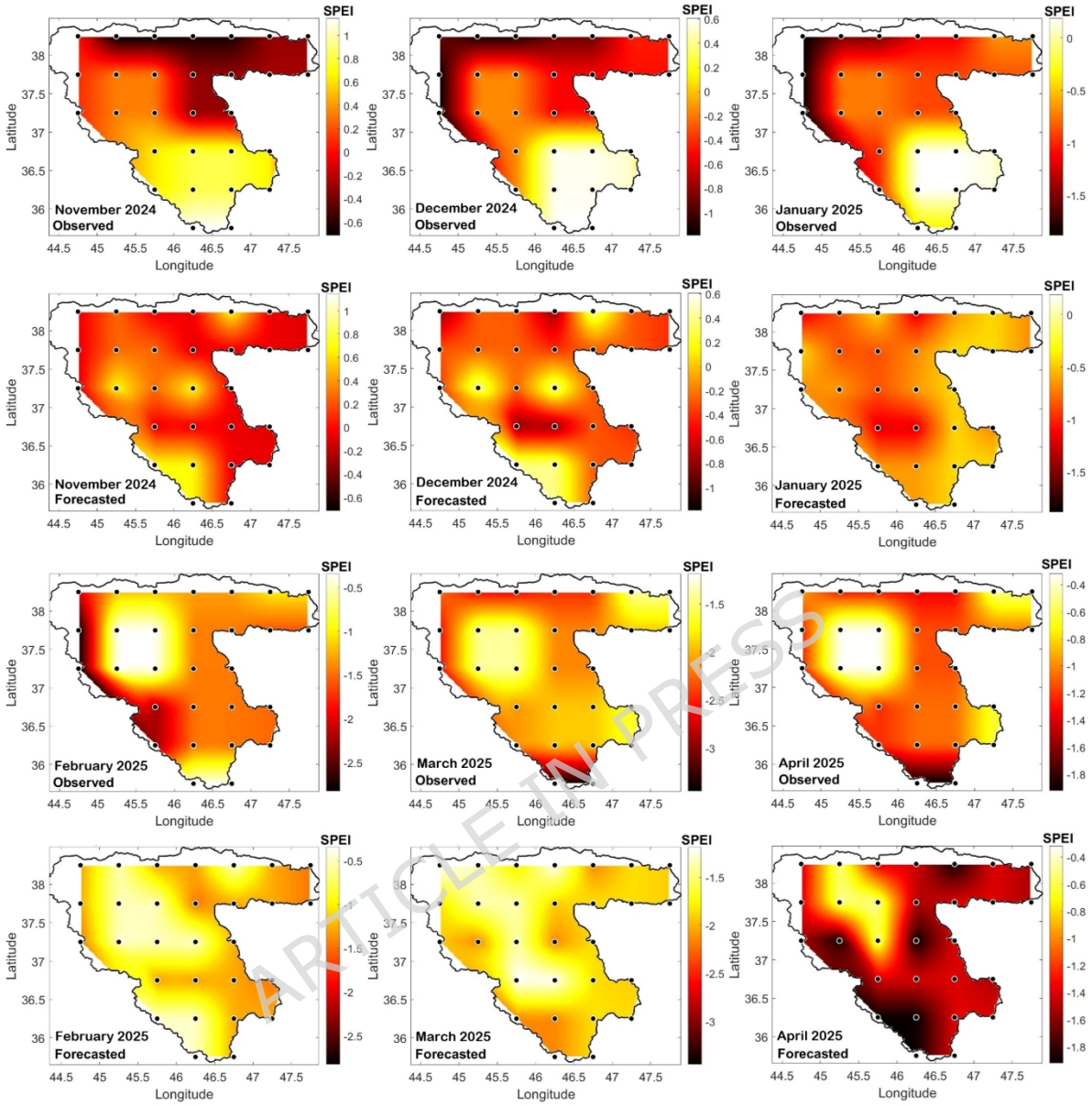
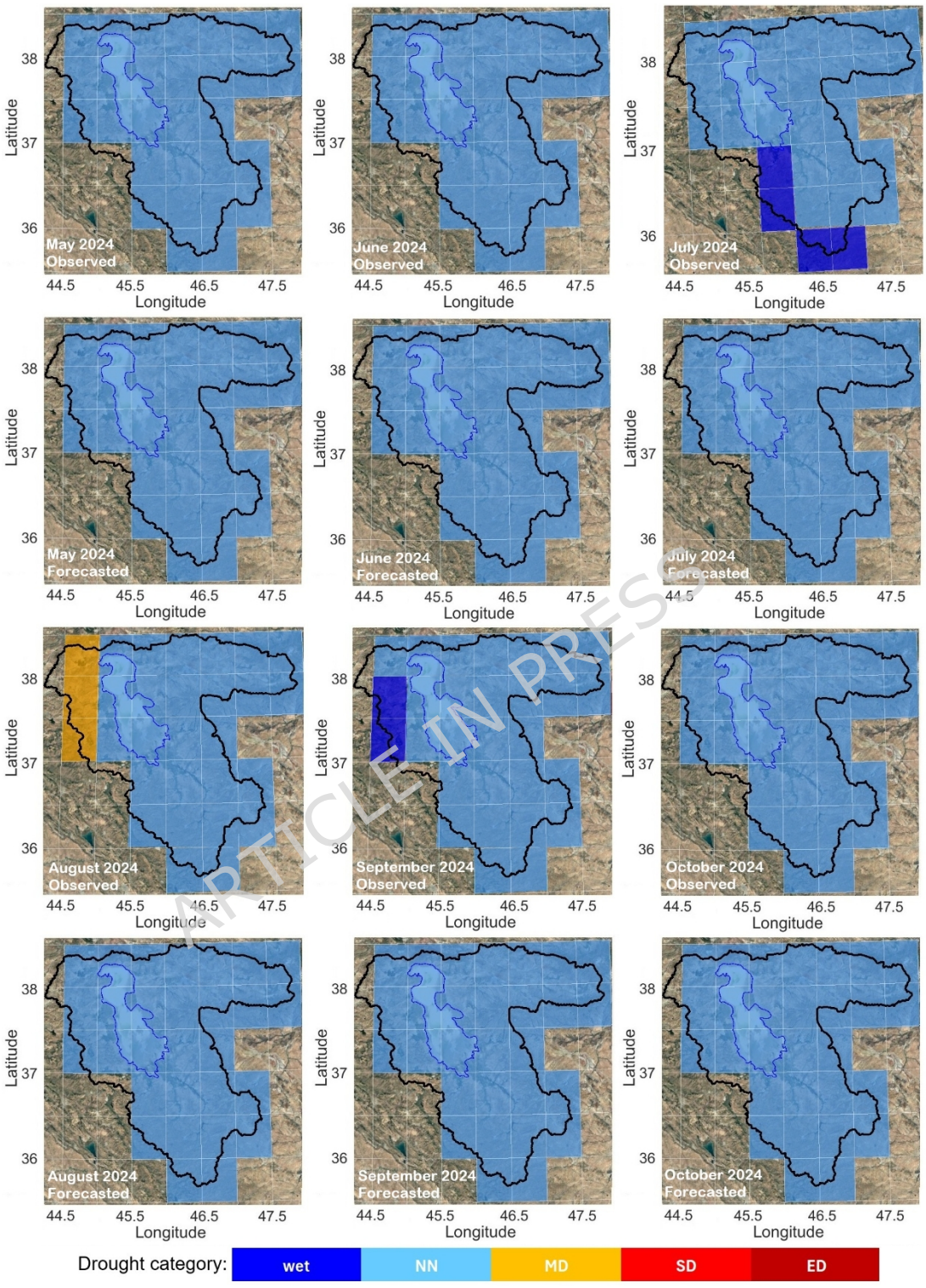


Figure 14. The observed and regionally forecasted SPEI-3 across the LUB for the last year of the testing period (May 2024 to April 2025; The maps were generated using MATLAB_R2023a).



ARTICLE IN PRESS

ARTICLE IN PRESS

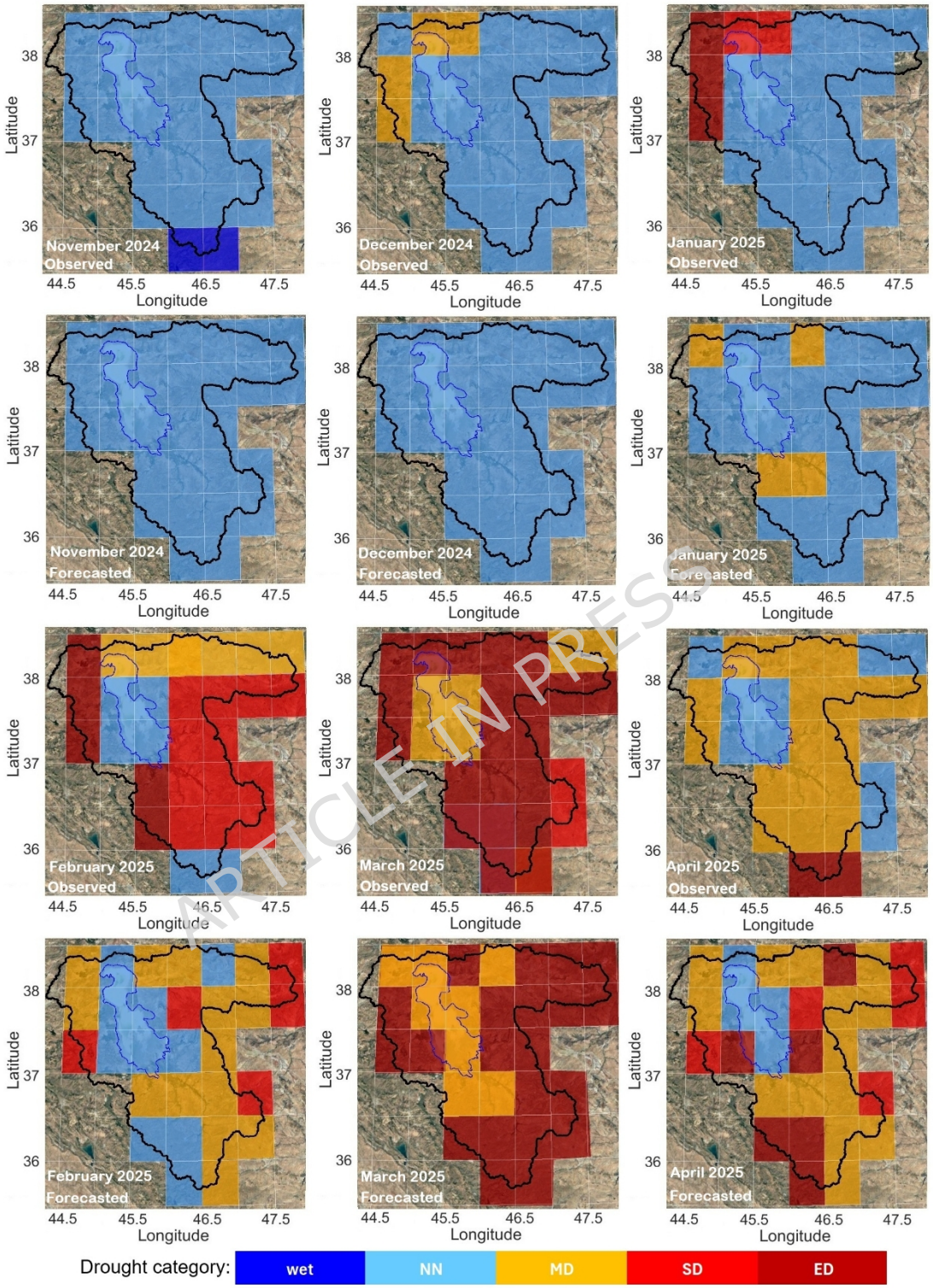


Figure 15. The observed and regionally forecasted drought categories across the LUB for the last year of the testing period (May 2024 to April 2025; The maps were generated using Google Earth Pro_7.3.71155).

ARTICLE IN PRESS

Table 8. Quantitative assessment of regional drought forecasting maps across the study area for the last year of the testing period (May 2024 to April 2025).

Month	RMSE	TA (%)
May 2024	0.538	100
June 2024	0.272	100
July 2024	0.349	86.2
August 2024	0.437	89.7
September 2024	0.433	93.1
October 2024	0.410	100
November 2024	0.607	93.1
December 2024	0.657	86.2
January 2025	0.620	72.4
February 2025	0.681	37.9
March 2025	0.669	65.5
April 2025	0.589	58.62
Mean:	0.522	81.89

ARTICLE IN PRESS

Table 8 provides a quantitative evaluation of the spatial accuracy of the RDF maps generated by the proposed MLNN model across the entire study area during the final year of the testing period (May 2024 to April 2025). The table reports monthly RMSE values and classification accuracy for each month, along with overall mean performance. The model demonstrates very high accuracy in the first half of the year, achieving perfect (100%) classification accuracy in May, June, and October 2024, and strong performance (86.2–93.1%) in the remaining summer and early autumn months, with RMSE values generally below 0.44. Accuracy remains satisfactory through November 2024 (93.1%), but declines noticeably during the winter and early spring months (January–April 2025), reaching a low of 37.9% in February 2025. This period of reduced performance coincides with higher RMSE values

ARTICLE IN PRESS

(0.620–0.681), likely reflecting greater challenge in capturing drought transitions or spatial heterogeneity during drier or more variable conditions. Despite these fluctuations, the overall mean classification accuracy across the 12-month period is 81.89%, with a mean RMSE of 0.522, indicating that the model provides good to very good spatial agreement with observed SPEI-based drought conditions over the full final year.

While Table 6 confirms the high regional accuracy of the MLNN model, its month-by-month performance reveals a tendency to underestimate drought intensity (Figure 14, Table 7). This highlights the particular challenge of forecasting short-term droughts like SPEI-3. Despite this limitation, the model's average spatial RMSE (≈ 0.47; extracted from Table 7) is notably lower than those of other DL approaches. For example, the state-of-the-art CNN-LSTM model by Danandeh Mehr et al. [64] reported higher RMSEs of 0.75 and 0.73 for the same task in two Turkish cities. Similarly, MLNN outperforms the transformer model suggested by Pathania and Gupta [24], which predicted the SPEI-3 values with an RMSE of 0.67 ± 0.08 across India at a lead time of one month.

ARTICLE IN PRESS

5. Novelty, implications, and limitations of the proposed method

The primary objectives of this study are twofold: (i) to develop a transferable, end-to-end methodology for RDF tailored to data-scarce or near-real-time constrained environments, where high-quality, gap-free station observations

ARTICLE IN PRESS

are often limited or delayed; and (ii) to generate continuous, gridded drought hazard maps with one-month lead time for basin-wide risk assessment and early warning systems.

5.1. Novelty

This study advances the field of drought forecasting by introducing an innovative integrated framework that addresses key gaps in operational tools for regional-scale applications, particularly in data-limited regions like LUB [15]. The main novel aspects include:

- First application of LNNs to drought forecasting: LNNs, a state-of-the-art continuous-time recurrent architecture, are employed here for the first time in modeling complex, non-linear temporal dependencies in SPEI time series. This represents a pioneering shift from conventional DL models (e.g., LSTM, which dominate SPEI forecasting studies) to more adaptive, efficient dynamics suited for hydrological sequences.
- Physically informed clustering for spatial homogeneity: An advanced clustering technique is used to delineate drought-homogeneous regions based on actual SPEI behavior, rather than arbitrary administrative or geographical boundaries. This ensures that LNN models are trained on spatially coherent patterns, enhancing physical plausibility, interpretability, and forecast accuracy while mitigating the "black-box" limitations often criticized in ML-based climate applications. Feature selection via MI and PCC

ARTICLE IN PRESS

further constrains inputs to the most relevant predictors, promoting more interpretable models.

- End-to-end operational workflow: The seamless integration of clustering, feature-selected LNN forecasting, and gridded RDF mapping creates a replicable blueprint for dynamic, near-real-time drought hazard assessment. This addresses the prevalent gap in operational tools, where existing approaches are typically static (based on historical data), station-scale, or limited to small catchments.
- Computational efficiency for large domains: By leveraging cluster representatives and compact LNN architectures, the framework overcomes persistent challenges in processing high-resolution, large-domain datasets, making it scalable for continental or multi-basin applications.

ARTICLE IN PRESS

These contributions provide a methodologically robust advancement, bridging isolated research prototypes with practical, deployable systems for proactive drought management.

5.2. Implications

The proposed framework marks a significant shift from static, historical drought risk maps to dynamic, one-month-lead forecasting using readily available real-time GDM SPEI series. This enables a transition from reactive disaster response to proactive risk management, resource allocation, and early warning in vulnerable basins like the LUB, where climate variability and

ARTICLE IN PRESS

overexploitation have drastically reduced lake surface area. Practically, the gridded RDF maps can serve as operational triggers in drought early warning systems. For example, forecasted SPEI drops below severe thresholds (e.g., -1.42) could automate alerts to stakeholders via SMS, apps, or portals, integrating seamlessly with existing national systems (e.g., Iran's FAO-supported agricultural drought monitoring platform). In the LUB, these forecasts—strongly correlated with lake levels and reservoir dynamics—support adaptive strategies such as adjusted irrigation scheduling to reduce over-extraction, conserve groundwater, and prioritize water allocations during predicted dry periods. Broader implications include enhanced resilience in semi-arid regions facing similar challenges, with potential for online dissemination of forecasts to inform policy, agriculture, and hydrological planning.

ARTICLE IN PRESS

5.3. Limitations

The methodology relies on the GDM SPEI-3 series, which incorporates GPCC precipitation data among other inputs. While this ensures reliability and real-time accessibility in data-scarce settings, global gridded products like GPCC (~0.5° resolution) introduce uncertainties, particularly in topographically complex or gauge-sparse areas such as parts of the LUB. Discrepancies with dense local observations have been noted in prior studies, constraining the maximum achievable accuracy of RDF outputs. Although the validation metrics (e.g., Table 7 and Figure 12) reflect realistic performance with these

ARTICLE IN PRESS

public datasets, bias-corrected global products remain a standard, scientifically robust choice when real-time station data are available. To diminish the associated uncertainties at high-risk clusters, identified in RDF maps (e.g., Figure 15), complementary site-specific modeling with in-situ data is recommended. Caracteizing uncertainties to the different parameter estimation methods, particulary evapotranspiration, can improve the results' reliability [65]. In practice, time series data are also subject to various distortions caused by environmental factors [66]. Effectively handling these distortions remains a key challenge in loss-function design for time series forecasting. To improve DL model performance while explicitly accounting for such data distortions, future research could adopt a semantic-aware loss-function framework.

In this study, model comparisons were limited to SARIMA; extending evaluations to other DL architectures (e.g., LSTM, Transformer-based models) would strengthen benchmarks. The deliberate focus on SPEI-3 provides hydrologically meaningful stability over shorter timescales (e.g., SPEI-1), but future work could explore multi-scale indices to capture varied drought responses. Additionally, performance may vary with training period length or subsets of the GDM-SPEI record, warranting future sensitivity analyses for robustness under different historical windows.

ARTICLE IN PRESS

6. Conclusion

Building on the robustness of the LNN technique for small datasets and its strong adaptability to nonstationary time series, this study introduced a novel approach for RDF using GDM-SPEI-3 time series, which is of important application for sustainable water resources and agricultural management at ungaged catchments. The new approach was implemented for one-month ahead drought forecasting across LUB, which has an area of more than 52000 km^2, presenting challenges in developing drought prediction maps using high-resolution gridded products due to the computational burden required for complex ML/DL algorithms over such a vast area. The proposed approach clustered the LUB into five centroids, each representing a unique cluster. An individual MLNN model was trained and tested for each cluster using the cluster representative SPEI-3 series, its own lags, and the cross-lags of exogenous series selected from the GDM point closest to the cluster centroid in both space and feature space. These trained models were then applied to corresponding cells across the region, capturing spatial variability of drought conditions at a 50-km resolution. The numerical and categorical forecasting accuracy demonstrated the efficiency of the new approach across the study area.

To secure practical applicability and reproducibility of similar works in other basins, we offered three new MATLAB scripts that are used for (i) determination of drought hemogeneous clusters using k-means method

ARTICLE IN PRESS

optimized by Silhouette analysis, (ii) one-step-ahead dynamic SARIMA modeling, and (iii) time series forecasting using LNN (a recurrent layer with learnable time constants) with user-defined inputs. Integration of the first and the third scripts resulted in a cluster-based MLNN, a valuable tool for RDF and mapping, which was applied for the first time in the water resources engineering community. Applying similar analytical ways to other regions is recommended to produce drought risk maps that support informed decision-making for sustainable water resource management and agricultural planning. To better account for long-term decision-making, multi-step-ahead forecasting scenarios can be designed with the proposed framework, which needs additional care for the inclusion of various sources of uncertainty. It is also recommended that forecasts be updated monthly, as is done by the GDM repository, thereby creating a dynamic mapping product that incorporates the most recent data. Followeing recent trend in the evolution of environmental models, evolution of interpretable models could provide more insight at large scale drought modeling.

ARTICLE IN PRESS

Funding Declaration

This work has been supported by the University of Tabriz, Vice Chancellorship for Research and Technology, International & Academic Cooperation Directorate, in the framework of Iranian Talents Joint Projects program.

ARTICLE IN PRESS

Software and Data Availability Statement

The GDM point data used in this study and three MATLAB scripts developed for (i) k-means clustering optimized by silhouette analysis, (ii) one-step-ahead recursive SARIMA modeling, and (3) time series forecasting using multivariate LNN are available at: GitHub-alidanandeh/regional_drought_forecasting_MLNN.

Author contributions

A.D.M. and A.A.G. designed the study. A.D.M. A.A.G. and R.T. performed the literature investigation. A.D.M. and R.T. analyzed the results. A.D.M. and A.A.G. wrote the initial manuscript and R.T. critically reviewed it. A.D.M. developed all the MATLAB scripts and supervised the research. All authors have read and approved the final version of the manuscript.

ARTICLE IN PRESS

References

1. Tabari, H., & Willems, P. (2018). More prolonged droughts by the end of the century in the Middle East. *Environmental Research Letters*, *13*(10), 104005.

2. Hameed, M., Ahmadalipour, A., & Moradkhani, H. (2020). Drought and food security in the middle east: An analytical framework. *Agricultural and Forest Meteorology*, *281*, 107816.

3. Khosravi, Y., & Ouarda, T. B. M. J. (2025). Drought risks are projected to increase in the future in central and southern regions of the Middle East. *Communications Earth and Environment*, 6(1), 384. https://doi.org/10.1038/s43247-025-02359-1

4. Trnka, M., Hlavinka, P., Možný, M., Semerádová, D., Štěpánek, P., Balek, J., ... & Žalud, Z. (2020). Czech Drought Monitor System for monitoring and forecasting agricultural drought and drought impacts. *International Journal of Climatology*, *40*(14), 5941-5958.

ARTICLE IN PRESS

5. Soylu Pekpostalci, D., Tur, R., Danandeh Mehr, A., Vazifekhah Ghaffari, M. A., Dąbrowska, D., & Nourani, V. (2023). Drought monitoring and forecasting across Turkey: A contemporary review. *Sustainability*, *15*(7), 6080.

6. Sun, J., Graf, R., Wrzesiński, D., Di Nunno, F., Luo, Y., Zhu, S., ... & Granata, F. (2025). Unveiling spatiotemporal patterns of compound hydrological droughts and river heatwaves in Poland. *Journal of Hydrology: Regional Studies*, *61*, 102621.

7. Madadgar, S., AghaKouchak, A., Shukla, S., Wood, A. W., Cheng, L., Hsu, K. L., & Svoboda, M. (2016). A hybrid statistical-dynamical framework for meteorological drought prediction: Application to the southwestern United States. *Water Resources Research*, *52*(7), 5095–5110. https://doi.org/10.1002/2015WR018547

8. Abbasi, A., Khalili, K., Behmanesh, J., & Shirzad, A. (2019). Drought monitoring and prediction using SPEI index and gene expression programming model in the west of Urmia Lake. *Theoretical & Applied Climatology*, *138*. 553–567.

9. Wu, Z., Yin, H., He, H., & Li, Y. (2022). Dynamic-LSTM hybrid models to improve seasonal drought predictions over China. *Journal of Hydrology*, *615*, 128706. https://doi.org/10.1016/j.jhydrol.2022.128706

10. Deo, R. C., Kisi, O., & Singh, V. P. (2017). Drought forecasting in eastern Australia using multivariate adaptive regression spline, least square support vector machine and M5Tree model. *Atmospheric Research*, *184*, 149–175. https://doi.org/10.1016/j.atmosres.2016.10.004

11. Danandeh Mehr, A., Vaheddoost, B., & Mohammadi, B. (2020). ENN-SA: A novel neuro-annealing model for multi-station drought prediction. *Computers and Geosciences*, 145, 104622. https://doi.org/10.1016/j.cageo.2020.104622

12. Özger, M., Mishra, A. K., & Singh, V. P. (2012). Long lead time drought forecasting using a wavelet and fuzzy logic combination model: A case study in Texas. *Journal of Hydrometeorology*, *13*(1), 284–297. https://doi.org/10.1175/JHM-D-10-05007.1

13. Mokhtar, A., Jalali, M., He, H., Al-Ansari, N., Elbeltagi, A., Alsafadi, K., et al. (2021). Estimation of SPEI Meteorological Drought Using Machine Learning Algorithms. *IEEE Access*, *9*, 65503–65523. https://doi.org/10.1109/ACCESS.2021.3074305

14. Lotfirad, M., Esmaeili-Gisavandani, H., & Adib, A. (2022). Drought monitoring and prediction using SPI, SPEI, and random forest model. *Journal of Water and Climate Change*, 13(2), 383-406.

15. Sureh, F. S., Sattari, M. T., Rostamzadeh, H., & Kahya, E. (2024). Meteorological drought assessment and prediction in association with

ARTICLE IN PRESS

combination of atmospheric circulations and meteorological parameters via rule based models. *Journal of Agricultural Sciences*, *30*(1), 61-78.

16. Al Mamun, M. A., Sarker, M. R., Sarkar, M. A. R., Roy, S. K., Nihad, S. A. I., McKenzie, A. M., et al. (2024). Identification of influential weather parameters and seasonal drought prediction in Bangladesh using machine learning algorithm. *Scientific Reports*, *14*(1), 566. https://doi.org/10.1038/s41598-023-51111-2

17. Adikari, K. E., Shrestha, S., Ratnayake, D. T., Budhathoki, A., Mohanasundaram, S., & Dailey, M. N. (2021). Evaluation of artificial intelligence models for flood and drought forecasting in arid and tropical regions. *Environmental Modelling & Software*, *144*, 105136.

18. Altunkaynak, A., & Çelik, A. (2023). Accurate extended time horizon drought prediction via wavelet-season-fuzzy models. *Applied Soft Computing*, *143*, 110432.

19. Danandeh Mehr, A., Ghavifekr, A. A., Ghazaei, E., Safari, M. J. S., Ke, C. Q., & Nourani, V. (2025). S-Transformer: a new deep learning model enhanced by sequential transformer encoders for drought forecasting. *Earth Science Informatics*, *18*(2), 341.

20. Zheng, C., Kim, H., LaJoie, E., He, S., & Chang, E. K. M. (2025). Improving Statistical Prediction of Subseasonal CONUS Precipitation Based on ENSO and the MJO by Training With Large Ensemble Climate Simulations. *Geophysical Research Letters*, *52*(2), e2024GL110925. https://doi.org/10.1029/2024GL110925

21. Suliman, A. H. A., Awchi, T. A., & Shahid, S. (2025). Integrating gridded precipitation data and machine learning for enhancing drought prediction in Iraq. *Modeling Earth Systems and Environment*, *11*(3), 1-11.

22. Zeng, J., Yuan, X., Yang, H., Ji, P., & Xu, X. (2025). Characterizing flash drought patterns in Eastern China based on high-resolution and long-term soil moisture fusion data. *Journal of Hydrology*, 133680.

23. Chen, X., & Dai, A. (2024). Quantifying contributions of external forcing and internal variability to Arctic warming during 1900–2021. *Earth's Future*, *12*(5), e2023EF003734.

24. Pathania, A., & Gupta, V. (2025). Interpretable transformer model for national scale drought forecasting: Attention-driven insights across India. *Environmental Modelling & Software*, *187*, 106394.

25. Abolafia-Rosenzweig, R., He, C., Chen, F., Ikeda, K., Schneider, T., & Rasmussen, R. (2023). High Resolution Forecasting of Summer Drought in the Western United States. *Water Resources Research*, *59*(3), e2022WR033734. https://doi.org/10.1029/2022WR033734

26. Wei, Z., Miao, L., Peng, J., Zhao, T., Meng, L., Lu, H., ... & Shi, J. (2024). Bridging spatio-temporal discontinuities in global soil moisture

ARTICLE IN PRESS

mapping by coupling physics in deep learning. *Remote Sensing of Environment*, *313*, 114371.

27. Luo, W., Qiu, H., Wei, Y., Huangfu, W., & Yang, D. (2025). A proposed method for landslide detection based on transfer learning and graph neural network. *Geoscience Frontiers*, 16(6), 102171.

28. Karbasi, M., Jamei, M., Malik, A., Kisi, O., & Yaseen, Z. M. (2023). Multi-steps drought forecasting in arid and humid climate environments: Development of integrative machine learning model. *Agricultural Water Management*, 281, 108210. https://doi.org/10.1016/j.agwat.2023.108210

29. Lee, S., Nourani, V., Danandeh Mehr, A., Moriasi, D., & Mirchi, A. (2024). Wavelet-Entropy Enhanced Clustering: A Comprehensive Analysis of Drought Patterns in the Southern Plains, United States. *Journal of Hydrometeorology*, *25*(12), 1809–1822. https://doi.org/10.1175/JHM-D-24

30. Mehrian, M. R., Hernandez, R. P., Yavari, A. R., Faryadi, S., & Salehi, E. (2016). Investigating the causality of changes in the landscape pattern of Lake Urmia basin, Iran using remote sensing and time series analysis. *Environmental monitoring and assessment*, 188(8), 462.

31. Okhravi, S., Eslamian, S., & Esfahany, S. T. (2017). Drought in lake urmia. In *Handbook of Drought and Water Scarcity* (pp. 605-618). CRC Press.

32. Safaie, A., & Jamaat, A. (2024). Numerical study of hydrodynamics and salinity transport processes in a hypersaline lake: A case study of Lake Urmia. *Advances in Water Resources*, 185, 104632.

33. Hassanzadeh, E., Zarghami, M., & Hassanzadeh, Y. (2012). Determining the main factors in declining the Urmia Lake level by using system dynamics modeling. *Water Resources Management,* 26(1), 129–145.

34. Vicente-Serrano, S. M., Beguería, S., & López-Moreno, J. I. (2010). A Multiscalar Drought Index Sensitive to Global Warming: The Standardized Precipitation Evapotranspiration Index. *Journal of Climate*, 23(7), 1696–1718. https://doi.org/10.1175/2009JCLI2909.1

35. Beguería, S., Vicente-Serrano, S. M., Reig, F., & Latorre, B. (2014). Standardized precipitation evapotranspiration index (SPEI) revisited: parameter fitting, evapotranspiration models, tools, datasets and drought monitoring. *International journal of climatology*, *34*(10), 3001-3023.

36. Zhang, Q., Liu, W., Yue, P., Zhang, L., Wang, S., Yang, J., ... & Yan, X. (2025). Discussion on Major Drought Issues in the Northern Drought-Prone Belt in China. *Bulletin of the American Meteorological Society*, *106*(4), E678-E706.

37. Chai, Y., Miao, C., AghaKouchak, A. et al. Flash droughts exacerbate global vegetation loss and delay recovery. *Nat Commun* (2025). https://doi.org/10.1038/ s41467-025-67173-x

ARTICLE IN PRESS

38. Lee, S., Moriasi, D. N., Mehr, A. D., & Mirchi, A. (2024). Sensitivity of Standardized Precipitation and Evapotranspiration Index (SPEI) to the choice of SPEI probability distribution and evapotranspiration method. *Journal of Hydrology: Regional Studies*, 53, 101761.

39. Liang, Y., Qiu, H., Wang, J., Zhu, Y., Zhao, K., Li, Y., ... & Kou, Y. (2025). Automated identification of ground kinematic patterns based on InSAR time series displacement and K-SC clustering. *Engineering Geology*, 108367.

40. Liu, H., Hu, M., & Yang, L. (2026). A directional flow pattern-driven framework for fine-grained air traffic flow prediction. *Aerospace Science and Technology*, 168, 111029.

41. Santos, J. F., Pulido-Calvo, I., & Portela, M. M. (2010). Spatial and temporal variability of droughts in Portugal. *Water Resources Research*, *46*(3), W03503. https://doi.org/10.1029/2009WR008071

42. Zhou, H., Zhou, W., Liu, Y., Yuan, Y., Huang, J., & Liu, Y. (2020). Meteorological drought migration in the Poyang Lake Basin, China: Switching among different climate modes. *Journal of Hydrometeorology*, *21*(3), 415–431. https://doi.org/10.1175/JHM-D-19-0183.1

43. Ji, J., Wang, J., Mou, Y., Long, C., & Wu, J. (2026). How to Break It Down for Building It Up? Theory-Guided Graph Decomposition Learning for Spatiotemporal Traffic Prediction. *IEEE Transactions on Pattern Analysis and Machine Intelligence*. 48 (5), 5442-5459.

44. Mehr, A. D., Shadkani, S., Abualigah, L., Safari, M. J. S., & Migdady, H. (2024). A novel stabilized artificial neural network model enhanced by variational mode decomposing. *Heliyon*, *10*(13).

45. Danandeh Mehr, A. & Gandomi, A. H. (2021). MSGP-LASSO: An improved multi-stage genetic programming model for streamflow prediction. *Information Sciences*, *561*, 181-195.

46. Hasani, R., Lechner, M., Amini, A., Rus, D., & Grosu, R. (2021, May). Liquid time-constant networks. In *Proceedings of the AAAI Conference on Artificial Intelligence* (Vol. 35, No. 9, pp. 7657-7666).

47. Hasani, R.; Lechner, M.; Amini, A.; Liebenwein, L.; Ray, A.; Tschaikowski, M.; Rus, D. Closed-form continuous-time neural networks. Nat. Mach. Intell. 2022, 4, 992–1003.

48. Karn, P. K., Ardekani, I., & Abdulla, W. H. (2024). Generalized framework for liquid neural network upon sequential and non-sequential tasks. *Mathematics*, *12*(16), 2525.

49. Wu, Y., Kang, H., Wang, W., Zhao, S., He, X., & Chen, J. (2025). Short-Term Highway Traffic Flow Prediction via Wavelet–Liquid Neural Network Model. *Modelling*, *6*(2), 39.

ARTICLE IN PRESS

ARTICLE IN PRESS

50. Hasani, R. M., Lechner, M., Amini, A., Rus, D., & Grosu, R. (2018). Liquid time-constant recurrent neural networks as universal approximators. *arXiv preprint arXiv:1811.00321*.

51. Danandeh Mehr, A., Sorman, A. U., Kahya, E., & Hesami Afshar, M. (2020). Climate change impacts on meteorological drought using SPI and SPEI: case study of Ankara, Turkey. *Hydrological Sciences Journal*, *65*(2), 254-268.

52. Valipour, M. (2015). Long-term runoff study using SARIMA and ARIMA models in the United States. *Meteorological Applications*, *22*(3), 592-598.

53. Hossain, M. A., Rahman, M. M., Hasan, S. S., Mahmud, A., & Bai, L. (2025). Analysis and forecasting of meteorological drought using PROPHET and SARIMA models deploying Machine Learning Technique for southwestern region of Bangladesh. *Environmental and Sustainability Indicators*, 100761.

54. Danandeh Mehr, A., Ghadimi, S., Marttila, H., & Torabi Haghighi, A. (2022). A new evolutionary time series model for streamflow forecasting in boreal lake-river systems. *Theoretical and Applied Climatology*, *148*(1), 255-268.

55. Su, R., Zhao, J., Bao, S., Fu, H., Wang, H., Zhang, X.,... Wu, X. (2025). Deep learning approach for internal tide prediction based on China Ocean Reanalysis data. *Ocean Engineering*, 340, 122348. doi: https://doi.org/10.1016/j.oceaneng.2025.122348

56. Zhang, Z., Wang, S., Ye, B., & Ma, Y. (2025). A feature prediction-based method for energy consumption prediction of electric buses. *Energy*, *314*, 134345.

57. Zhang, Q., Liu, H., Li, L., Li, Y., Liu, Z., & Sun, Z. (2026). A real-time prediction model for tunnel rock strength using geological drilling data and physics-informed neural networks. *Tunnelling and Underground Space Technology*, *170*, 107272.

58. AghaKouchak, A., Norouzi, H., Madani, K., Mirchi, A., Azarderakhsh, M., Nazemi, A., ... & Hasanzadeh, E. (2015). Aral Sea syndrome desiccates Lake Urmia: call for action. *Journal of Great Lakes Research*, *41*(1), 307-311.

59. Tourian, M. J., Elmi, O., Chen, Q., Devaraju, B., Roohi, S., & Sneeuw, N. (2015). A spaceborne multisensor approach to monitor the desiccation of Lake Urmia in Iran. *Remote Sensing of Environment*, *156*, 349-360.

60. Ghorbani-Aghdam, M., Dinpashoh, Y., & Mostafaeipour, A. (2013). Application of factor analysis in defining drought prone areas in Lake Urmia Basin. *Natural hazards*, *69*(1), 267-277.

ARTICLE IN PRESS

61. Fazel, N., Berndtsson, R., Uvo, C. B., Madani, K., & Kløve, B. (2018). Regionalization of precipitation characteristics in Iran's Lake Urmia basin. *Theoretical and Applied Climatology*, *132*(1), 363-373.

62. Liu, Q., Bao, S., Yan, H., Wang, H., Wang, Y., & Zhang, R. (2025). Enhancing sea surface salinity short-term prediction using physically informed deep learning. *Applied Ocean Research*, 165, 104832.

63. Dikshit, A., Pradhan, B., & Alamri, A. M. (2021). Long lead time drought forecasting using lagged climate variables and a stacked long short-term memory model. *Science of the Total Environment*, *755*, 142638. https://doi.org/10.1016/j.scitotenv.2020.142638

64. Danandeh Mehr, A., Rikhtehgar Ghiasi, A., Yaseen, Z. M., Sorman, A. U., & Abualigah, L. (2023). A novel intelligent deep learning predictive model for meteorological drought forecasting. *Journal of Ambient Intelligence and Humanized Computing*, *14*(8), 10441-10455.

65. Zhao, Y., Wang, H., Song, B., Xue, P., Zhang, W., Peth, S., ... & Horn, R. (2023). Characterizing uncertainty in process-based hydraulic modeling, exemplified in a semiarid Inner Mongolia steppe. *Geoderma*, *440*, 116713.

66. Liao, H., Liu, X., Guo, L., Yuan, L., & Chen, Q. (2026). Time series forecasting with semantic-aware trend loss function. *IEEE Internet of Things Journal*. 13 (7), 12687-12701.

ARTICLE IN PRESS